

Analyzing the dust of the Nearby Universe

Author: Jimmy Kjellqvist

30 credit Master's thesis

Department of Physics and Astronomy, Uppsala University

Supervisor: Jens Jasche

Local supervisor: Martin Sahlén

Subject reviewer: Erik Zackrisson

August 29, 2021



UPPSALA
UNIVERSITET

Abstract

The aim of this master thesis is to investigate the influence of intergalactic dust on astronomical observations. The current cosmological paradigm of an accelerating cosmic expansion is supported by observations of Type Ia supernovae. However, the light emitted by these and other cosmological sources is not only redshifted by cosmic expansion but will also interact with matter along the light path which affects the light. Especially intergalactic dust can lead to additional reddening and dimming of distant sources due to light scattering or absorption. This yields systematic contaminations to cosmological measurements. Using quasars as backlight sources we seek to estimate the attenuation of their observed spectra caused by intergalactic dust in order to determine the existence and properties of the intergalactic dust. In this thesis we will analyse the methods and tools used as well as discussing the dust properties and how they affect the results. This thesis shows that intergalactic dust exist, and has a notable effect on cosmological measurements and favors dust grains consisting of silicate with a size around $0.1 \mu\text{m}$ with Ω_{dust} around $5 - 7 \times 10^{-6}$. The conclusion is in agreement with previous studies of the same matter. With the increasing precision of cosmological measurements systematic effects such as intergalactic dust is a factor that has to be taken into account.

Sammanfattning

Syftet med denna masteruppsats är att undersöka de effekter intergalaktiskt stoft har på astronomiska observationer. Den ledande kosmologiska modellen som säger att universum expanderar är stöttad av observationer av Typ 1a supernovor. Ljuset som kommer från supernovorna är däremot inte bara påverkade av den kosmiska expansionen men kommer också interagera med materia på vägen som påverkar ljuset. Speciellt intergalaktiskt stoft kan leda till ytterligare dimning av ljuset och att ljuset blir rödare. Detta är på grund av spridningen eller absorptionen av ljuset när ljuset interagerar med stoftpartiklarna. Detta leder till systematiska fel i kosmologiska mätningar. Genom att använda kvasarer som en ljuskälla försöker vi uppskatta ljusdämpningen på deras spektrum som orsakats av intergalaktiskt stoft. Detta görs för att bestämma ifall intergalaktiskt stoft existerar och vad dess egenskaper är. I denna uppsats gjordes en analys av metoden, beräkningsverktygen som användes och några egenskaper hos stoft. Slutsatsen av denna analys visar på att intergalaktiskt stoft existerar och har en mätbar effekt på kosmologiska observationer. Resultatet visar att modellen föredrar stoft av silikat med storlekar runt $0.1 \mu\text{m}$ med Ω_{dust} runt $5 - 7 \times 10^{-6}$ vilket stämmer överens med tidigare studier. Med den ökade pressionen av kosmologiska mätningar blir systematiska effekter, som den från intergalaktiskt stoft, ännu viktigare att ta i hänsyn.

Acknowledgements

I would like to start by thanking the Cosmo-AI group at Stockholm University for making me feel very welcomed to the group and made working from distance easier to overcome. Thank you for all of the weekly planning sessions and rewarding discussions about mine and everybody's projects. Thanks to Adam for the encouraging words and guidance. Especially thanks to my supervisor Jens Jasche for this great and interesting project, as well as all of the feedback and guidance throughout the project.

Thanks to my local supervisor Martin Sahlén and my subject reviewer Erik Zackrisson for valuable feedback and support with the thesis. Additional thanks to my examiner Andreas Korn for the administrative support and feedback.

A huge thanks to my friends and family for being supportive through this thesis. A special thanks to my partner Felicia and my parents for being extra supportive and being my pillars of stability.

This thesis used an image from Antonucci 2013. Reprinted by permission from Robert Antonucci: Nature Antonucci 2013

Contents

1	Introduction	7
2	Stellar evolution	8
2.1	Low-mass stars	10
2.2	Mid-sized stars	10
2.2.1	Subgiant phase	11
2.2.2	Red giant & the horizontal branch	11
2.2.3	Asymptotic giant branch (AGB) phase	12
2.2.4	Post-AGB phase	12
2.3	Massive stars	12
3	Our expanding universe	13
3.1	The cosmological model	14
3.2	Measuring the expansion of the universe with supernovae	15
3.3	Comoving frame of reference	16
4	Photometry and photometric systems	16
4.1	Effective wavelength	16
4.2	Bandwidth (FWHM)	17
4.3	SDSS filters	17
4.4	Magnitudes	18
4.5	Colour	19
5	Intergalactic dust and their influence on cosmological measurements	19
5.1	Sources of dust	19
5.2	Intergalactic dust	20
5.3	Potential dust types	20
5.4	X-ray scattering	21
5.5	Dust extinction	21
5.5.1	Comoving number density of dust	22
5.5.2	Dust scattering & absorption cross section	22
5.5.3	Optical depth of intergalactic dust	23
6	Using quasars as back light sources	24
6.1	A Quasi-Stellar Object (QSO)	25
6.2	Properties of QSO's	26
7	Method & Result	27
7.1	The experimental setup	27
7.2	Simulating quasars as the back light sources	27
7.2.1	The composite spectrum	28
7.2.2	Possible contamination in the generation of the composites	30
7.3	Applying dust attenuation to the back light sources	31
7.3.1	Constraining the total amount of all dust grains	31
7.3.2	Constraining total mass of all dust grains	31
7.3.3	Integrating the line-of-sight optical depth of intergalactic dust	32
7.3.4	Predicting dust attenuated quasar spectrum	32
7.4	Discussion of the dust attenuation model	34
7.4.1	The distribution and number density of intergalactic dust	34
7.4.2	The properties of dust, their structure and cross section	36

7.4.3	The dependency of optical depth on model parameters	36
7.4.4	Dust attenuated quasar spectra	36
7.5	Comparing predictions to observed quasar colours	36
7.5.1	Observed quasar colours	37
7.5.2	Predicted quasar colours	38
7.5.3	Comparing simulations to observations	39
7.6	Testing colour calculations with varying degree of complexity	41
7.6.1	1. Baseline spectrum	41
7.6.2	2. Composite spectrum with no dust attenuation	42
7.6.3	3. Composite spectrum with dust attenuation with constant cross-section	42
7.6.4	4. Composite spectrum with dust attenuation	42
7.6.5	Conclusion from the testing	43
7.7	Discussion of colour comparison	43
7.8	Analyzing parameters to fit simulations to observations	44
8	Discussion of the statistical analysis and findings	46
9	Conclusion & summary	46
10	Outlook & prospects	47
A	Results of Model 1	52

1 Introduction

Cosmological observations suggests that the universe is expanding at an accelerated rate (Hubble 1929). This expansion is supported by observations of Type Ia supernovae which have well-defined luminosity properties and lightcurves resulting in that they can be used as standard candles (Riess et al. 2016). In an expanding universe the lightcurves produced by these standard candles would be shifted towards the red part of the spectrum due to the light travelling through expanding space, resulting in a cosmological redshift. The further away they are the further shifted towards the red the lightcurves are since the space the light travels through has undergone greater expansion. However there are other factors which could induce a redshift of the lightcurves. One of these factors are the matter the light interact with along the path to us, especially intergalactic dust can lead to additional reddening and dimming of distant sources due to the light being scattered or absorbed and re-emitted by the dust grains (Johansson 2015). The interaction between the light and the dust grains thus yield a systematic contamination in cosmological measurements. In Figure 1 we can see how cosmic dust reddens the light from sources behind the cosmic dust. This contamination could contribute to the discrepancy between differently attained cosmological constants (Mortsell et al. 2021).

Cosmic dust can spawn from various sources. These sources include Type II supernovae, Asymptotic Giant Branch (AGB) stars, galaxy and star formation, etc. However for the dust to dilute the intergalactic media the dust needs to leave its origins and the galaxies from which they were born. To be able to do this the dust must have acquired sufficient kinetic energies in their making such that they can escape the potential well of the galaxy. This means that supernovae are potential producers of intergalactic dust since the dust created in such events can be ejected with great kinetic energies. With time more and more supernovae and other astronomical processes which produces dust will occur thus enriching the intergalactic medium (IGM) with dust over time (Johansson and Mörtzell 2012).

Cosmic dust is also a key ingredient in understanding the formation and evolution of stars, since stars are formed in regions full with dust as well as cosmic dust being important for many evolutionary steps of stars (Karttunen H. et al. 2017). Dust also plays a role in the formation of galaxies and their evolution. So in order to gain better understanding of both stars and galaxies knowledge about cosmic dust plays a big part. Lets summarize why cosmic dust is important:

- It plays a big role in the formation and evolution of stars.
- It is key to understanding galaxy formation and evolution.
- It causes a reddening of sources behind the dust.
- As the precision of cosmological measurements increases systematic effects, such as those from intergalactic dust, plays a larger role.
- It could help to understand the gap in the Hubble tension.

In this thesis we investigate the influence of intergalactic dust on observations, as well as constraining the properties of intergalactic dust such as the dust grain size. We do this by constructing a forward model where we model a simulated quasar spectrum after which we apply our intergalactic dust attenuation model onto the spectrum. Once we can generate intergalactic dust attenuated quasar spectra we compare these to SDSS data of observed quasars by comparing the colours of the simulations and the observed data. We then fit the input parameters of the dust model to the SDSS data by doing a statistical analysis of several different dust models with varying parameters. This thesis assumed further simplifications

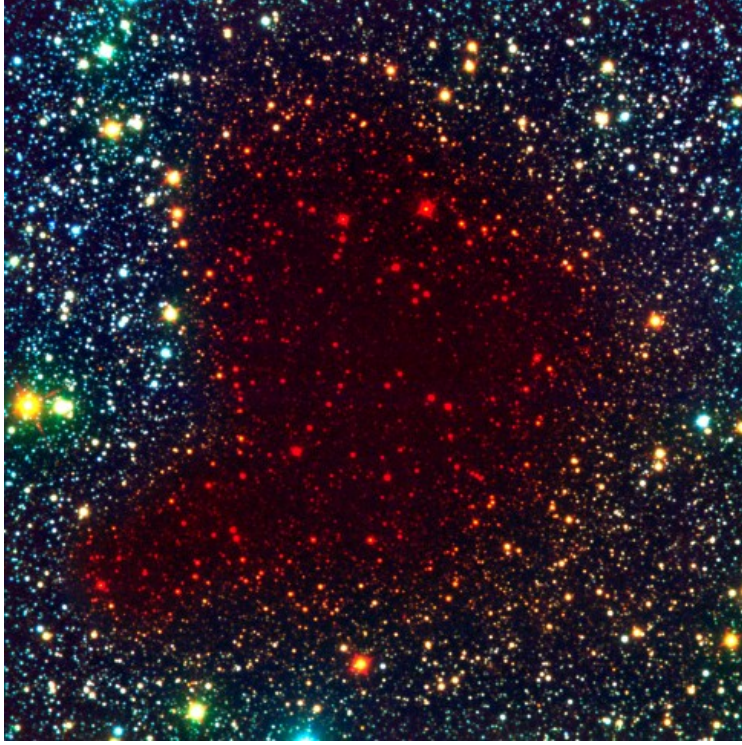


Figure 1: A Bok globule which is a dense region of cosmic dust and gas where star formation may take place. As seen in the image the cosmic dust cloud reddens the light from the sources behind the dust cloud. Image source: *Bok globule B68*, ESO 2001

of the model that was initially planned not to be included, more on this in Section 8. Parts of this thesis is an updated version of previous work (Kjellqvist 2021).

Let me end the introduction with the inspirational quote from Carl Sagan:

“Even through your hardest days, remember we are all made of stardust.” - Carl Sagan

2 Stellar evolution

When investigating intergalactic dust and its influence on observations, especially over different redshift, it is necessary to take the production of dust into consideration and how that has changed the number density of dust grains over time. The creation of intergalactic dust grains are mainly linked to different evolutionary stages of stars (Masataka Fukugita 2011, Gall, Hjorth, and Andersen 2011), so lets take a look at stellar evolution.

All stars are formed from collapsing clouds of gas and dust. These massive clouds are often called molecular clouds or nebulae. These protostars contract over the course of millions of years until they finally enters a state of equilibrium and enters the so called Main-Sequence (MS). How long a star spends on the MS depends on the mass of the star, where more massive stars are shorter lived compared to less massive. In Table 1 lifespans for an array of masses (Bertulani 2013).

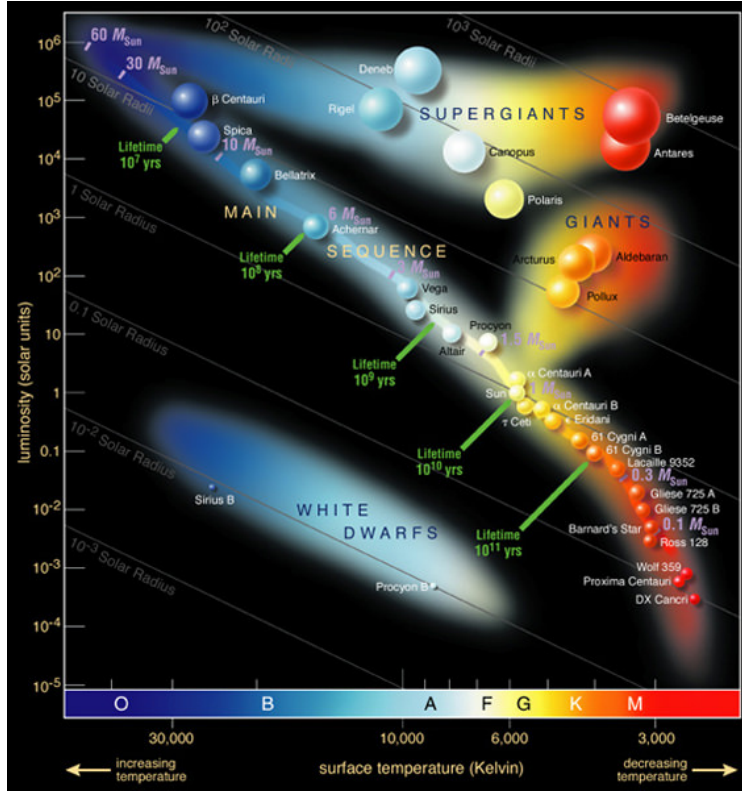


Figure 2: The evolutionary tracks of stars along the MS shown in a Hertzsprung-Russel (HR) diagram. The evolution of the stars depends on where they start on the MS. In the plot sun is seen on the MS in the yellow part. The giant and supergiant stars are also seen in the diagram, as well as the white dwarfs. Image source: *Main Sequence, Universe Today* 2010.

Mass (solar masses M_{\odot})	Time [years]	Spectral type
60	3 million	O3
30	11 million	O7
10	32 million	B4
3	370 million	A5
1.5	3 billion	F5
1	10 billion	G2 (Sun)
0.1	1000s billions	M7

Table 1: The lifetime of stars with different masses along with their spectral type (Bertulani 2013). The spectral type is a classification based on spectral characteristics of the star, which depends on the temperature of the star, O being the coolest and M the hottest.

Nuclear fusion is what powers the stars during the majority of their existence. Initially this is via fusion of hydrogen into helium in the core of MS stars. As the hydrogen is consumed in the core the star will start to move away from the MS. How the star moves through and beyond the MS depends on the mass of the star. One can thus divide the stars into low ($<0.6 M_{\odot}$ (solar mass)), mid ($0.6-8 M_{\odot}$) and massive ($>8 M_{\odot}$) sized (Iben 1967).

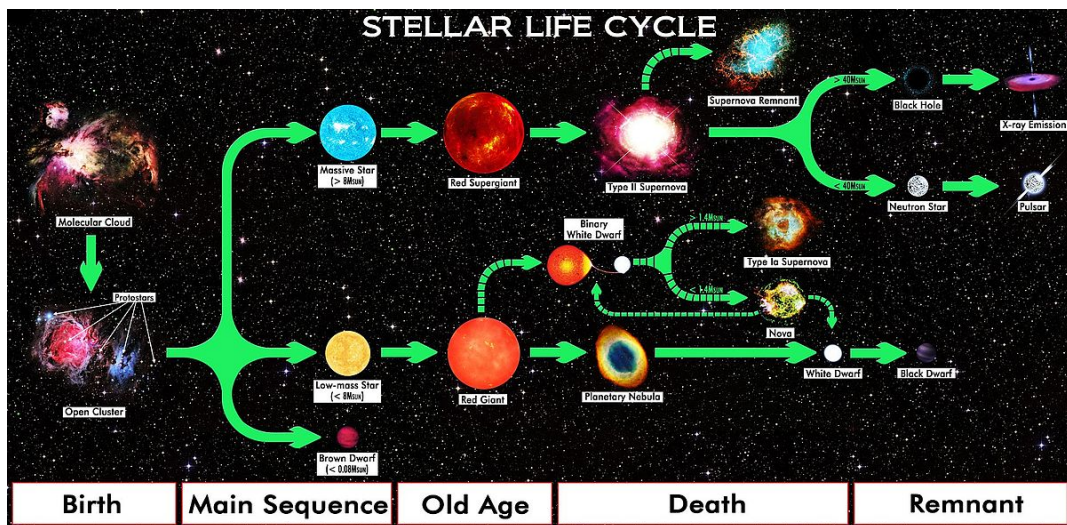


Figure 3: The entire stellar life cycle for different mass stars, starting from the birth in the molecular clouds and ending with the remnants. Image source: *Star Life Cycle Chart*, R.N. Bailey 2017

2.1 Low-mass stars

Due to the extremely long lifespan of low-mass stars we have not observed what happens to these stars once they stop producing energy through fusion. Since the universe is around 13.8 billion years old and the lifespan of these stars are sometimes several orders of magnitudes larger we can only investigate the evolution of these stars through theoretical models and computer simulations. Models of red dwarfs with a mass of $0.1 M_{\odot}$ suggest that the such stars will stay on the MS for around six to twelve trillion years. During this period they would gradually increase in both temperature and luminosity, and finally moving of the MS taking several hundred billion years to collapse into a white dwarf, thus never evolving into a red giant (F. Adams, P. Bodenheimer, and G. Laughlin 2005).

Stars which are slightly more massive will eventually expand into red giants but their cores will not become massive enough to reach the temperatures required for burning of helium thus never reaching the tip of the red giant branch (see Figure 4). These stars will also eventually collapse into white dwarfs (Gregory Laughlin, Peter Bodenheimer, and F. C. Adams 1997).

2.2 Mid-sized stars

Mid-sized stars go through several stages during their evolutionary track. Figure 4 shows their evolutionary track through the HR diagram along with a brief explanation of each phase.

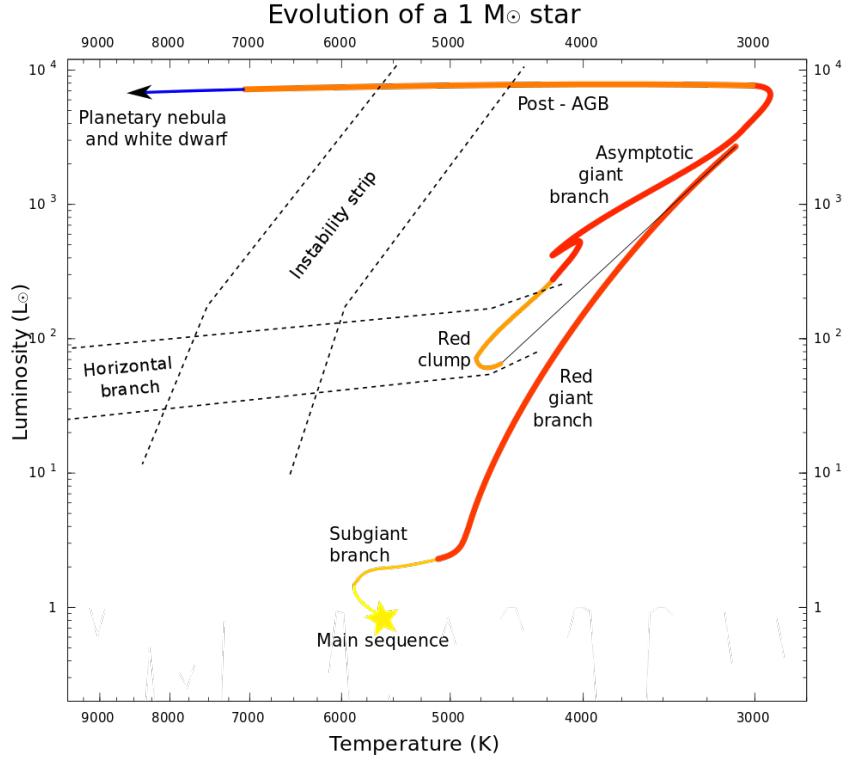


Figure 4: The evolutionary track of a $1 M_{\odot}$ star shown in a HR diagram. It starts at the main sequence moving into the subgiant branch, then into the red giant branch eventually reaching the Asymptotic giant branch (AGB), and lastly reaching the post AGB phase and ending as a planetary nebula and a white dwarf. Image source: *Evolutionary track, Lithopsian 2016*

2.2.1 Subgiant phase

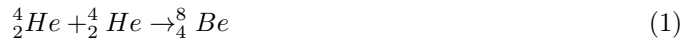
Once the hydrogen in the core of MS stars are depleted the stars leave the MS and enters the subgiant phase. In this phase the star begins to fuse hydrogen in a shell around its helium core, continuously increasing the mass of the core as more helium is created in the shell. During this period the star expands and cools. This process occurs over a period of several million to one or two billion years depending on the mass of the helium core. As the convective envelope of the star expands it will eventually begin to increase in temperature and luminosity and expand into the red giant branch (Ryan and Norton 2010).

At a certain point the helium core becomes sufficiently massive such that fusion of helium begins.

2.2.2 Red giant & the horizontal branch

How the star evolves in the red giant phase is highly dependent on the mass of the star. For stars with masses $\leq 2.3 M_{\odot}$ their cores will continue to grow and increase in density to a point where it becomes degenerate, meaning that the electron degeneracy pressure becomes significant due to the Pauli exclusion principle. This will lead to a uniform temperature increase, due to the high conductivity of the degenerate gas, eventually reaching 100 million degrees which is sufficient for helium burning to start via the triple alpha process (Equations 1 and 2). The sudden start of helium burning will occur simultaneously throughout the entire

core which will lead to a great increase in temperature. Due to the core being degenerate it will not expand leading to a greater increase in temperature which only accelerates the fusion of helium. Eventually the temperature reaches a point where the electron degeneracy pressure is not required to keep the core from collapsing, which removes the degeneracy of the gas. This causes the core to expand rapidly and only a couple of seconds after the start of helium burning there is an explosion, the so called *helium flash* (Karttunen H. et al. 2017).



This might sound flashy (is puns allowed in a master thesis?), but the energy released in the explosion is absorbed by the outer layers and turned into potential energy of the core, which eventually leads to a non-degenerate core which burns helium into carbon. After the helium flash the star reaches the horizontal branch, which gets its name from the fact that the luminosity does not change much while the temperature may vary (Karttunen H. et al. 2017).

For stars with a mass in the $2.3\text{--}8 M_{\odot}$ range the temperature of the cores is greater than the temperature of the smaller star's cores. They also have less dense cores, which results in the core never entering a stage of degeneracy. This means the cores can start their helium burning in a non-catastrophic way which does not result in a helium flash (Karttunen H. et al. 2017).

2.2.3 Asymptotic giant branch (AGB) phase

Once the helium is depleted in the core the core will consist of carbon and oxygen. At this point a helium layer will form outside of this core where helium burning will continue. Outside of this helium layer a layer of hydrogen exists where hydrogen burning continues. During this stage the star will move in a similar track as it did during the red giant phase, but at higher temperatures, thus it is called the asymptotic giant branch. During this phase the energy production of the star is dominated by either the hydrogen or the helium shell in an alternating fashion. Once sufficient helium has been created in the hydrogen shell it will drop down to the helium shell igniting more rapid burning of helium. A star with two different layers of fusion is an unstable one and the star enters a *thermally pulsing phase* where material will periodically be ejected into space. This leads to the creation of a lot of dust (Karttunen H. et al. 2017, Sackmann, Boothroyd, and Kraemer 1993, Gall, Hjorth, and Andersen 2011).

2.2.4 Post-AGB phase

These pulsations and stellar winds will continue until all of the star's outer layers are expelled as a planetary nebula. These planetary nebulae are rich of heavy elements such as carbon and oxygen, and as it moves away from the star it cools allowing the creation of dust particles and molecules to take place. The remaining star never becomes hot enough to start carbon and oxygen burning, resulting in the star cooling down and becoming a white dwarf consisting of carbon and oxygen (Karttunen H. et al. 2017, Gall, Hjorth, and Andersen 2011).

2.3 Massive stars

There are some similarities between the evolution of intermediate mass stars and massive stars, but there are some very clear differences. Generally the more massive a star is the faster all of the evolutionary processes occur and the shorter it is lived. This shorter life-span leads to massive stars being more difficult to find, and is usually found in young galactic

structures. Massive stars start, as for any other star, with hydrogen burning in their core. As that is depleted the star leaves the MS and starts to expand into a supergiant. They also start to burn helium in their core in a non-catastrophic manner in contrast to lower mass stars. They also differ from lower mass stars in that they are able to fuse elements beyond helium, meaning that they do not eject their outer layers through shell burning of hydrogen and helium. Instead they continuously fuse heavier and heavier elements starting with carbon and then oxygen and silicon burning, creating layers after each burning process is completed. In each layer the burning of that element continues. The most massive stars, larger than $15 M_{\odot}$, are able to fuse elements all the way to ^{56}Fe creating onion-like structures with several shells with different material where shell burning occurs. These are not stable structures and will eventually lead to a collapse of the star when the core exceeds the Chandrasekhar limit of about $1.4 M_{\odot}$. At this point the electron degeneracy pressure is not enough to overcome the gravitational pull (Karttunen H. et al. 2017).

During the collapse the core will collapse on a faster time scale compared to the outer layers. The collapse results in a great increase in temperature in the outer layers where unburnt nuclear fuel resides. This leads to a runaway fusion reaction resulting in explosive burning releasing great amounts of energy in a core collapse supernova supernovae. The majority of the energy are in the form of neutrinos, but great amounts of matter is also ejected leading to the creation of dust (Karttunen H. et al. 2017, Gall, Hjorth, and Andersen 2011).

The very dense collapsing core will finally either turn in to a neutron star, a star consisting almost entirely of neutrons in a degenerate state due to the extreme pressure, or a black hole depending on if the mass exceeds the Tolman-Oppenheimer-Volkoff limit (Karttunen H. et al. 2017).

3 Our expanding universe

Since we will investigate the influence of intergalactic dust on a cosmological scale we have to take the expansion of the universe into account. In 1929 Hubble detected that far away galaxies seemed to be moving away from us with a recession velocity (Hubble 1929). This was noted due to the galaxies appearing redder than they should, implying that a Doppler shift towards the red part of the spectrum has occurred. A solution to these velocities were proposed saying that the universe is expanding. This resulted in Hubble's law, $v = H_0 d$, where v is the recession velocity, H_0 is Hubble's constant and d is the distance to the light source. Hubble's constant are in units $\text{km s}^{-1} \text{Mpc}^{-1}$ and measures the expansion rate of the universe as a function of distance (Riess et al. 2016).

For nearby objects their redshift may originate from peculiar velocities, like velocities due to gravitational influences. In contrast to redshift, where objects move away from us, sometimes the objects may be moving towards us leading to a blueshift (Barbara Ryden 2006a). However at larger distances the redshift occurs due to the expansion of space in between us, the observer, and the object we are observing. This cosmological redshift depends on how much the space has expanded since the light we observed was emitted, and can be calculated with

$$1 + z = \frac{a(t_0)}{a(t)}, \quad (3)$$

where z is the cosmological redshift, $a(t)$ is the cosmological scale factor which describes how much the universe has expanded as a function of time. t is the time when the light was emitted and t_0 is the time when it was observed. One can use the cosmological scaling factor

to describe the Hubble parameter $H(t)$ (Barbara Ryden 2006a),

$$H(t) \equiv \frac{\dot{a}(t)}{a(t)}, \quad (4)$$

where $\dot{a}(t)$ is the time derivative of the scaling factor. Calculations of data from Cepheid variables and other astrophysical sources have determined the local value of the Hubble constant to be $73.24 \pm 1.74 \text{ km s}^{-1} \text{ Mpc}^{-1}$ (Johansson 2015, Riess et al. 2016). There are however a second method of calculating the Hubble constant using the *Planck* satellite and inferring the constant from lensing measurements of the Cosmic Microwave Background. The interesting part is that this second method infers a value of about $H_0 \approx 67 \text{ km s}^{-1} \text{ Mpc}^{-1}$, hence differing from the inferred value from Cepheids. The tension between the two different measurements of the same "constant" is a known problem, or mystery, within cosmology since it still is unclear why the measurements differ (Wu et al. 2020). It could be a sign of new physics but it could also be a sign of so far unknown systematic effects in the data analysis. Recent studies suggest that inaccurate colour-luminosity calibration caused by extinction from dust denies the precision required to claim a substantial tension between the two methods Mortsell et al. 2021.

3.1 The cosmological model

Our cosmological model builds upon Einstein's theory of general relativity which describes the 4-dimensional space time structure of the universe and how it evolves. This evolution depends on the matter distribution of the universe, and the interaction between time and matter (i.e space-time) is explained in Einstein's field equations (Einstein 1916). One can apply various cosmological models for different universes to the field equations and it would result in equations that would describe how that universe evolves as well as how matter and time would interact with each other. The cosmological model that best fits our universe postulates the so called *cosmological principle*. The cosmological principle states that the spatial distribution of matter in the universe, on large scales, is both *isotropic* as well as *homogeneous*. This means that on large scales the universe looks the same at every location and at every angle. Astronomer William Keel stated:

"The cosmological principle is usually stated formally as 'Viewed on a sufficiently large scale, the properties of the universe are the same for all observers.' This amounts to the strongly philosophical statement that the part of the universe which we can see is a fair sample, and that the same physical laws apply throughout. In essence, this in a sense says that the universe is knowable and is playing fair with scientists." - William C. Keel 2007

The Friedmann-Lemaitre-Robertson-Walker (FLRW) model assumes the cosmological principle for a simple matter distribution. Applying the FLRW model to Einstein's field equations results in the Friedmann equations which describes the dynamics of the universe (Friedmann 1922),

$$H^2 = \left(\frac{\dot{a}}{a}\right)^2 = \frac{8\pi G\rho}{3} - \frac{k}{a^2} \quad (5)$$

and

$$\left(\frac{\ddot{a}}{a}\right) = -\frac{4\pi G}{3}(\rho + 3p) \quad (6)$$

where H is the Hubble parameter, a the cosmological scale factor, G is the gravitational constant, ρ and p is the total energy density and total pressure of the Universe respectively, and k is the curvature of the Universe.

Here it often is useful to divide the total energy density of the Universe into its contributing parts, $\rho = \rho_m + \rho_\Lambda + \rho_r$. Here m signifies matter, which can be divided into dark and baryonic matter, Λ signify dark energy, and r which signify relativistic matter, meaning radiation. An equation of state parameter can be introduced for each of these parameters, $\omega \equiv p/\rho$ where

$$\rho = \rho_0 a^{-3(1+\omega)}. \quad (7)$$

For matter (both baryonic and dark matter) the energy density is zero resulting in $\omega_m = 0$, for radiation $\omega_r = 1/3$ and for dark energy $\omega_\Lambda = -1$. Normalizing this density to the critical density of the universe we can now introduce the density parameter $\Omega = \rho/\rho_{crit}$, where $\rho_{crit} \equiv 3H^2/8\pi G$ is the critical density of the universe (the density required for a flat universe, i.e $k = 1$). The density parameter, Ω , essentially describes what the universe is made of by describing how large the contribution of a certain component is compared to the total energy density. Together these parameters for the different components of the universe decide the evolution and dynamics of the universe. Now using Equation 7 and the density parameter one can express Equation 5, and the Hubble parameter, as

$$H(z)^2 = H_0^2 [\Omega_r(1+z)^4 + \Omega_m(1+z)^3 + \Omega_\Lambda], \quad (8)$$

which is a useful expression when calculating cosmological distances (Barbara Ryden 2006b).

In order to measure the density parameters one usually either observe how structure grow or by measuring distances. There are two main ways of measuring cosmological distances. One is using standard candles, which are objects with known intrinsic brightness, and you look at how the lightcurves have changed (for example redshifted, how much dimming etc). The other method is using object with known physical size, otherwise known as standard rulers. If one observes a standard ruler they can deduce the distance to them by looking at the angular size of the object in the sky (Barbara Ryden 2006b). In this paper we will mainly consider the standard candles.

3.2 Measuring the expansion of the universe with supernovae

One of the most useful type standard candles are Type Ia Supernovae (SNe Ia) due to their standardized lightcurves. A Type Ia supernova occurs when there is a close binary between a white dwarf and a companion star where matter is accreted to the white dwarf until it reaches Chandrasekhar limit of about $1.4 M_\odot$ (Mazzali et al. 2007). When this limit is reached the electron degeneracy pressure is not enough to overcome the gravitational pull and the white dwarf collapse. The increase in temperature and density results in an explosive fusion reaction which then destroys the white dwarf. The majority of the energy released is in the form of kinetic energy of the ejecta and is of the order of 10^{44} J. The radiation energy, which is around 10^{42} J, arises from the fusion of ^{56}Ni into radioactive cobalt and then eventually into stable iron (Karttunen H. et al. 2017). About 20 days after the explosion the SNe reaches it's peak brightness, of about $M_B = -19.3$ magnitudes in the B-band (more about photometry in the next chapter), after which the supernovae quickly fades. Hamuy et al. 1995 and Phillips 1993 found that there is a correlation between the peak intrinsic brightness and the rate of decline following the maximum, namely that brighter supernovae have a slower decline. This along with the fact that brighter supernovae tend to be bluer (Tripp 1998) leads to the possibility of corrections of the lightcurve. There are several algorithms that performs these corrections to the shape and color of the lightcurves. Once this is done the SNe can be used as a standard candle and help constrain cosmological parameters along with other probes, such as the Cosmic Microwave Background and Baryon Acoustic Oscillations.

However there are several uncertainties when it comes to measurements of SNe and their use in cosmology. One of these uncertainties are the intergalactic dust the light from the SNe has to interact with on the way.

3.3 Comoving frame of reference

When discussing cosmological densities, such as the number density of galaxies, intergalactic dust grains, stars etc. it is advantageous to discuss them in a comoving frame of reference as will become apparent later. This is a frame of reference which expands with the expanding universe meaning that a particle which is at rest has a fixed comoving coordinate which is constant with time. Take this in contrast to a particle's physical coordinates, which is the distance you would measure if you froze time and laid out a ruler. A particle's physical distance increase with time due to the expansion of space. When converting between physical coordinates and comoving coordinates we are interested in the scale factor at the coordinates of interest. Thus using a comoving coordinate system is especially advantageous when analysing densities. In physical coordinates the density is proportional to the cube of the scale factor, a^{-3} , meaning that through the history of the universe the expansion of space is likely the main contributor to the change of density. We can thus factor the change in density from cosmic expansion out by looking at a comoving coordinate system. In this system any change to the density is the result of some "real" astrophysical effect and not just due to the expanding universe.

4 Photometry and photometric systems

Because we are going to use data from SDSS which uses photometry and photometric filters to do their measurement we have to discuss photometry a bit. Photometric filters are used by telescopes in astronomical surveys to select the wavelengths to observe. The filter transmits one portion of the spectrum to the detector in the telescope and dismisses any other. In other words, they are band-pass filters.

Transmission curves are a good representation of the behavior of these filters. Transmission curves essentially describe how efficiently the filter transmits light from a certain wavelength. There are two parameters that sufficiently describe the transmission curves. These are the effective wavelength ($\lambda_{effective}$) and the bandwidth, or otherwise known as the Full Width at Half Maximum (FWHM). Both of these parameters will be described in more detail in the following sections.

4.1 Effective wavelength

The effective wavelength is essentially the same as the isophotal wavelength (King 1952). The definition of isophotal wavelength is given in (Tokunaga and Vacca 2005) as:

A source with the intrinsic spectral distribution $F_\lambda(\lambda)$ cause N_p number of photoelectrons per second inside the detector in a telescope. These photoelectrons are then detected and N_p is described as:

$$N_p = \frac{1}{hc} \int F_\lambda(\lambda) S(\lambda) d\lambda \quad (9)$$

where h is Plancks constant, c is the speed of light in vacuum and $S(\lambda)$ is described by

$$S(\lambda) = T(\lambda)Q(\lambda)R(\lambda)A_{tel} \quad (10)$$

and is the total system response. Where $T(\lambda)$ describes the atmospheric transmission (i.e. disturbances from the atmosphere), $Q(\lambda)$ describes the quality of the telescope setup, $R(\lambda)$

describes how good the filter is at transmitting light at a certain wavelength and A_{tel} is the area of the mirror collecting light in the telescope. Because of the mean value theorem for integration and the fact that $F_\lambda(\lambda)$ and $S(\lambda)$ are both continuous and $S(\lambda)$ is always positive there exists a λ_{iso} such that

$$F_\lambda(\lambda_{iso}) \int \lambda S(\lambda) d\lambda = \int \lambda F_\lambda(\lambda) S(\lambda) d\lambda \quad (11)$$

where λ_{iso} is the isophotal wavelength. If we then rearrange Equation 11 we get

$$F_\lambda(\lambda_{iso}) = \frac{\int \lambda F_\lambda(\lambda) S(\lambda) d\lambda}{\int \lambda S(\lambda) d\lambda} = \langle F_\lambda \rangle \quad (12)$$

where $\langle F_\lambda \rangle$ is the mean value of the intrinsic flux of the source outside of the atmosphere across the bandwidth of the filter. This means that λ_{iso} is the wavelength where the mean flux across the bandwidth equals the monochromatic flux $F_\lambda(\lambda_{iso})$. This leads to λ_{iso} being the wavelength that best represents the filter, or the transmission curve. Or in other words, "the instrument acts effectively as if all the light were concentrated at this wavelength" (quote from King 1952). As mentioned earlier λ_{iso} is essentially the same as $\lambda_{effective}$.

4.2 Bandwidth (FWHM)

The Full Width at Half Maximum (FWHM) describes the bandwidth over which the filter transmits the light. Meaning it is an interval of wavelengths where the lower and upper limit is defined as the wavelength where the filter achieves 50% of its maximum transmission. The light with a wavelength inside the bandwidth gets transmitted and the light with a wavelength outside gets dismissed.

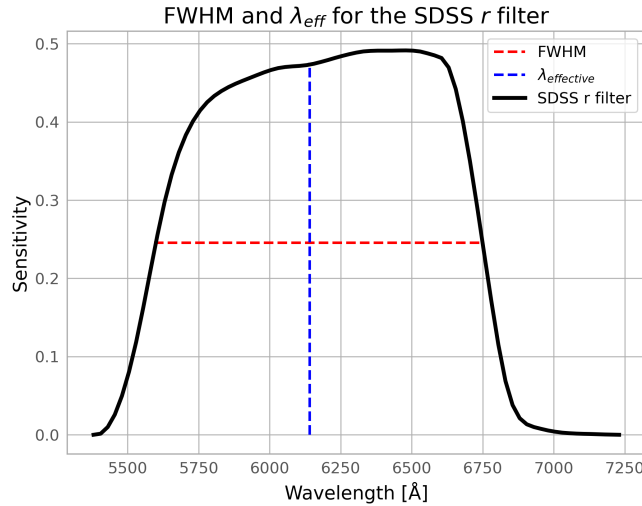


Figure 5: Illustration of the Full Width Half Maximum (FWHM) and the effective wavelength, λ_{eff} , for the SDSS r filter.

4.3 SDSS filters

There exists several different filters and photometric systems used in different surveys that want to look at different parts of the spectrum. Some may be interested in far infra-red

features and use appropriate filters for that, and some may be interested in UV features and hence use different filters. In this thesis we will use data obtained in the SDSS surveys. As such the data is given in magnitudes for the different SDSS filters. Below is a table containing the effective wavelength and bandwidth of the SDSS filters as well as a plot showing all of the transmission curves.

Filter	$\lambda_{effective}$ [Å]	FWHM [Å]
u	3557	599
g	4825	1379
r	6261	1382
i	7672	1535
z	9097	1370

Table 2: The effective wavelength and the FWHM for the different filters used in the SDSS survey as described in (M. Fukugita et al. 1996).

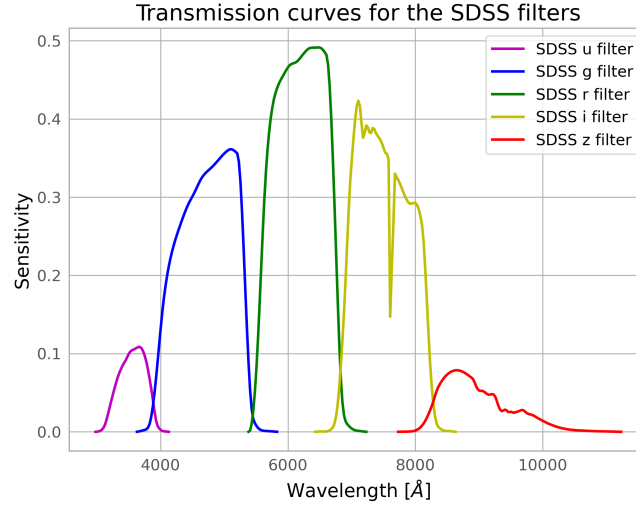


Figure 6: Illustration of the Full Width Half Maximum (FWHM) and the effective wavelength, λ_{eff} , for the SDSS r filter.

4.4 Magnitudes

Since humans perceive brightness, or change in brightness, on a logarithmic scale, astronomers have implemented the magnitude system. It is basically a logarithmic scale of the flux a star emits and it is calibrated to a certain star with a known brightness or some other calibration flux. Pogson's definition of apparent magnitudes is defined by the equation

$$m = -2.5 \log_{10} \left(\frac{F}{F_0} \right), \quad (13)$$

where F is the flux of the object and F_0 is the calibration flux. Sometimes a calibration star is used (often Vega). Instead of Vega one can use several stars or some calibrated absolute unit of flux as in the AB magnitude system. When there are several filters looking at different wavelengths one often has to calibrate the magnitude separately for each filter due to the

difference in sensitivity for the different filters for the instrument. The magnitude system is designed such that a magnitude 1 star is exactly 100 times brighter than a magnitude 6 star. This means that the lower the magnitude the brighter the object is and each magnitude step changes the brightness by a factor of $\sqrt[5]{100}$ (Karttunen H. et al. 2017). One can then convert the fluxes observed through photometric filters to magnitudes for that corresponding filter. Notice however that the SDSS magnitudes differ slightly from Pogson magnitudes, especially for low signal to noise sources (M. Fukugita et al. 1996).

4.5 Colour

For any photometric system with multiple coloured filters one can define colour indices. The colour index is the difference in magnitude between two filters, taking the magnitude for the lower wavelength filter and subtracting the higher wavelength filter magnitude. Thus the smaller the colour index is the more blue the object is and conversely the larger the index is the redder the object is (Karttunen H. et al. 2017). Colours are a useful measure to compare observations to simulations with since it is a logarithmic difference of the fluxes of a spectrum. This allows removing any systematic factors which are applied evenly over the entire spectrum. Below is a derivation showing that any constant factor k that is evenly multiplied with the spectrum gets removed.

$$\begin{aligned} m_x - m_y &= 2.5 \log_{10} F_y k - 2.5 \log_{10} F_x k \\ &= 2.5 (\log_{10} F_y + \log_{10} k - \log_{10} F_x - \log_{10} k) \\ &= 2.5 (\log_{10} F_y - \log_{10} F_x), \end{aligned} \tag{14}$$

where Equation 13 was used, x and y are two different filters and m is their magnitudes, $m_x - m_y$ is their colour, k is the constant, and F is their zero point corrected fluxes.

5 Intergalactic dust and their influence on cosmological measurements

The light emitted from distant objects may encounter several obstacles on the way, other galaxies, stars etc. However the majority of the time the light travels in the IGM, and on its path through the IGM the light may encounter dust grains. The existence of dust grains in the IGM has been a subject of great interest, and several studies have inferred a significant amount of intergalactic dust in the range of dust density $\Omega_{dust} \sim 10^{-6} - 10^{-5}$ (Loeb and Haiman 1997; Inoue and Kamaya 2004; Masataka Fukugita 2011). When it comes to intergalactic dust we are mainly interested in its interaction with light. There are several ways light can interact with dust. Dust grains can re-emit incoming UV and optical photons in the infrared to far-infrared. Dust grains are also able to scatter the X-rays from point sources with small scattering angles producing extended, diffuse halos instead of point sources. Additionally, some theoretical models predict the existence of small, rapidly rotating dust grains. If these dust grains have electric dipole moment there will be rotational emission emitting at microwave frequencies (Johansson 2015, B. T. Draine 2003a).

5.1 Sources of dust

The currently prevailing theories state that the producers behind dust are Core-Collapse (CC) supernovae (SNe) and Asymptotic Giant Branch (AGB) stars. As has been mentioned previously stars in their AGB phase undergoes strong stellar winds which can eject up to $10^{-4} M_{\odot} year^{-1}$ in their late stages. During the AGB phase the star may lose up to $\sim 80\%$

of their mass in the form of these stellar winds containing gas and dust. However it takes a long time for a star to evolve in to the AGB phase of its life, meaning that AGB stars are unlikely a contributor to dust at high redshift (Johansson 2015, Masataka Fukugita 2011, Gall, Hjorth, and Andersen 2011).

Core Collapse SNe is a potential contributor to the existence of dust at high redshifts. CC SNe occurs for large stars which have a shorter lifespan thus CC SNe is not as limited by time as AGB stars. There have been several studies providing strong evidence that CC SNe produces dust, contrary to Type Ia SNe which has strong evidence not to contribute any dust production (Johansson 2015).

To summarize: during the early period of the universe (towards high redshift) the main producers of dust is highly likely CC SNe, since the universe has not been around long enough for a significant amount of AGB stars to have formed. In contrast to later periods of the universe (lower redshifts) the main producers of dust will likely tip more towards AGB stars, since at later stages of the universe AGB stars become more abundant compared to massive stars that leads to CC SNe. This is partly because the lifespans of the two, where massive stars leading to CC SNe have a significantly lower lifespan compared to AGB stars. This results at lower redshifts the only CC SNe that occur are from relatively new born stars, while AGB stars are older stars coming from several different generations. Xiang et al. 2018 looked into stellar mass distribution and star formation history of the galactic disc and confirms that there are more $M_{\odot}pc^{-3}$ for older stars with ages over 1 billion compared to the ones younger than 1 billion. Another factor favoring AGB stars is the fact that stars tend to be less massive. It is very rare for stars to accumulate enough mass to incur a CC SNe (Karttunen H. et al. 2017).

5.2 Intergalactic dust

The existence of interstellar dust within galaxies has long been known. The existence of intergalactic dust, however, is under more debate. There have been numerous studies conducted surrounding the existence of intergalactic dust and several of them have inferred roughly the same intergalactic dust density, $\Omega_{dust} \sim 10^{-6} - 10^{-5}$, from estimates of how stellar density and metallicity depends on redshift (Loeb and Haiman 1997, Masataka Fukugita 2011, Inoue and Kamaya 2004).

There have also been studies surrounding the optical effects of intergalactic dust and observational proof of its existence, e.g reddening, extinction etc (short summary Johansson 2015).

One problem that intergalactic dust faces is that it must escape the potential well that is the gravitational field of the host galaxy where the originator star resides. There are several ways this could occur. The dust could be expelled from the originator with sufficient velocity due to radiation pressure such that they escape the potential well. During galaxy mergers interstellar dust may be expelled into the IGM or due to ram pressure as the galaxy moves through the IGM (Bianchi and Ferrara 2005; Aguirre 1999). This results in the composition of intergalactic dust differ from that of interstellar dust since intergalactic dust are more weighted towards heavier grains. Larger grains often result in less reddening and higher values of R_v , and are often labeled as "grey" dust.

5.3 Potential dust types

From examining meteorites and investigating how dust grains interact with light, one can deduce what these grains are made of. Draine (B. T. Draine 2003a) made a short list of likely candidates for interstellar dust grains based on the observations just mentioned. It was concluded that silicates, which are any anion consisting of silicone and oxygen, are a major

contributor to the total mass of interstellar dust. Carbonaceous materials, or materials which mainly consist of carbon, were also a prominent group of materials, in particular graphite as indicated by the 2175 Å feature in the spectrum of quasars. There are also other materials like SiC and carbonates which is not as prominent (B. T. Draine 2003a). J. S. Mathis, Rumpl, and Nordsieck 1977 found that graphite was a necessary component to any dust grain mixture, in order to achieve the correct spectral features. Graphite along with any other silicates proved to be a successful mixture in reproducing the interstellar extinction of the Milky Way, with a size distribution of graphite from $0.005 \mu m$ to $1 \mu m$ and silicates from $0.025 \mu m$ to $0.25 \mu m$. This distribution followed the power law $dn/da \propto a^{-k}$ with k ranging between $3.3 - 3.6$. However since intergalactic dust is weighed towards larger grains, as discussed in the previous section, we find a different dust size range for those. A intergalactic dust model that was found to be viable had a distribution of either silicate or graphite, or a mixture of both, with grain sizes in the range $0.25 \mu m$ to $0.05 \mu m$. So for our model we assume a composition of either silicate or graphite.

5.4 X-ray scattering

It has been shown that intergalactic dust grains may produce halos of scattered light around X-ray sources on cosmological distances due to X-ray scattering. The properties of the halo may provide us with information about the intergalactic dust causing the halo (John S. Mathis and Lee 1991, Smith and Dwek 1998, B. T. Draine 2003b). The differential cross section of the scattering interaction can be calculated using the Rayleigh-Gans approximation for a spherical dust grain with the radius a using the following equation (from Hayakawa 1970; Mauche Gorenstein 1986):

$$\frac{d\sigma_{scatter}}{d\Omega} = A_E \left(\frac{a}{1.0\mu m} \right)^6 \left[\frac{j_1(x)}{x} \right]^2 (1 + \cos^2\theta). \quad (15)$$

Here $x = (4\pi a/\lambda)\sin(\theta/2)$, j_1 is the spherical Bessel function of the first order $j_1(x) = (\sin x)/x^2 - \cos(x)/x$ and A_E is a normalization constant which depends on the energy E of the X-rays interacting with the dust grains and the grain composition. A_E can be calculated using the following equation:

$$A_E = 1.1 \left(\frac{2Z}{M} \right)^2 \left(\frac{\rho_{grain}}{3gcm^{-3}} \right) \left(\frac{F(E)}{Z} \right)^2, \quad (16)$$

where ρ_{grain} is the mass density of the dust grains, Z and M is the atomic number/charge and mass number respectively and $F(E)$ is the atomic scattering factor which depends on the X-ray energy (Henke, Gullikson, and Davis 1993). We see that Equation 15 only depends on the wavelength/energy of the X-rays, the scattering angle, and dust grain properties. If we know the source of the X-rays and their energies and look at the halo produced to deduce the scattering angle we are able to gather some information about the properties and amount of the dust grains which the X-rays interact with. The central core of this equation is also approximately Gaussian with the root mean square (rms) of the scattering angle indicating typical sizes of the scattered halo, $\theta_{rms} \approx 62.4(1.0\mu m/a)(1keV/E)\text{arcsec}$ (Johansson 2015).

5.5 Dust extinction

Light might undergo extinction due to scattering or absorption of the light when it encounters dust grains (see Figure 10). Light which has been affected by extinction are often linearly polarized since extinction are polarization-dependant requiring that some dust grains are aligned with the local magnetic field. Often extinction leads to reddening of the light,

which is an important factor when it comes to standard candles, where redshift is used as a distance measurement. This means that extinction of the light produces an offset of distance measurements towards greater distances. Thus, in order to make accurate measurements one has to take into account light extinction due to dust in the line of sight (Johansson 2015, B. T. Draine 2003a, Johansson and Mörtzell 2012).

The total to selective extinction ratio can be estimated by the ratio:

$$R_V \equiv \frac{A_V}{E(B - V)} = \frac{A_V}{A_B - A_V} \quad (17)$$

where $E(B - V)$ is the colour excess, and A_V and A_B is the extinction in the V- and B-band respectively. R_V could be seen as the "reddening parameter" or the slope of the extinction curve in the optical region and can be used to examine how much extinction has occurred (Johansson 2015, Johansson and Mörtzell 2012). When examining the effect of dust on measurements through dust extinction there are two key factors to take into consideration. One is the number density of dust grains between the observer and the object of interest. The other one is the extinction cross section, e.g with a given amount of dust grains how likely is it that a photon will interact with a dust grain on its path.

5.5.1 Comoving number density of dust

Since intergalactic dust spawns from stars we make the assumption that we can derive the comoving number density of intergalactic dust from the comoving star formation rate. This is one of our main assumptions of the model. The star formation rate, $\dot{\rho}_*(z)$, given in Hernquist and Springel 2003 is used. We then introduce a normalization factor, n_0 , such that

$$n(z) = n_0 \int_z^\infty dz' \frac{\dot{\rho}_*(z')}{(1+z')\varepsilon(z')}, \quad (18)$$

where $\varepsilon(z) = \frac{H(z)}{H_0} = \sqrt{\Omega_r(1+z)^4 + \Omega_m(1+z)^3 + \Omega_\Lambda}$ is the dimensionless Hubble parameter from Equation 8 (note that Ω_r is very small in comparison to Ω_m and Ω_Λ , making it negligible). We essentially normalize the integral such that n_0 is the comoving number density at redshift 0. We can thus relate n_0 to the present dust density of the universe Ω_{dust} through (Johansson and Mörtzell 2012)

$$\Omega_{dust} = (n_0 \frac{4\pi}{3} a^3 \rho_{grain}) / \rho_{crit}, \quad (19)$$

where a is the radius of the dust grain which is assumed to be spherical. ρ_{grain} is the density of the dust grain and $\rho_{crit} = 1.88 \times 10^{-29} h^2 \text{ g cm}^{-3}$ is the critical density of the universe. We can now rearrange the above equation to

$$n_0 = \frac{\Omega_{dust}}{a^3} \frac{3\rho_{crit}}{4\pi\rho_{grain}}. \quad (20)$$

Now for a given Ω_{dust} we can calculate the n_0 for a particular dust size and dust composition. In Figure 7 we see the normalized comoving number density of dust.

5.5.2 Dust scattering & absorption cross section

The geometrical cross section is the probability of a photon interacting with a dust grain, taking into account the size of the grain and the probability of dust-photon interactions. The cross section for a particular wavelength, λ , can be calculated as

$$\sigma(\lambda) = \pi a^2 Q(\lambda), \quad (21)$$

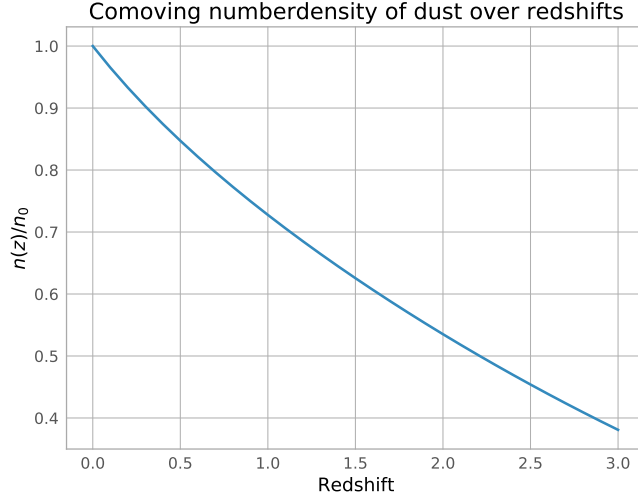


Figure 7: The evolution of the comoving number density of intergalactic dust. As can be seen there is a greater amount of dust towards lower redshifts. This should come as no surprise since the universe is continuously enriched with dust.

where a is the radius of the dust grains which are assumed to be spherical, Q is the sum of the efficiencies of the interactions due to scattering and absorption. Throughout this thesis a composition of silicates and graphite will be assumed for the intergalactic dust. From J. S. Mathis, Ruml, and Nordsieck 1977 we know the sizes of dust grains, and the sum of the efficiencies from Laor and Bruce T. Draine 1993 is used for silicates and graphite. In Figure 8 we see the data from Laor and Bruce T. Draine 1993 showing the silicate and graphite efficiencies. Not that these are laboratory results and not astronomical measurements.

5.5.3 Optical depth of intergalactic dust

Given the previous discussion we can now estimate the optical depth. The total optical depth due to scattering and/or absorption due to interactions with dust grains between redshift 0 and z_{obs} can be calculated with the following formula:

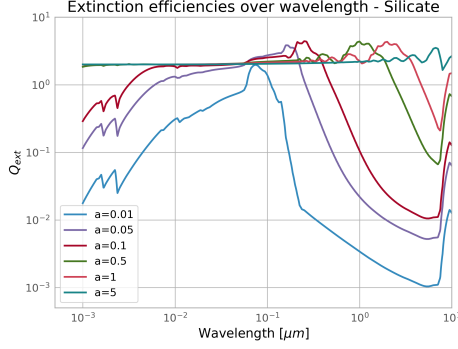
$$\tau(\lambda_{obs}, z_{em}) = \frac{c}{H_0} \int_0^{z_{em}} \frac{n(z')\sigma(\lambda')(1+z')^2}{\varepsilon(z')} dz', \quad (22)$$

where $\sigma(\lambda')$ is the geometrical cross section and $n(z')$ is the comoving number densities of the dust grains from the previous sections and $\lambda' = \lambda_{obs}/(1+z)$. For the sake of this thesis we assume dust to consist of homogeneous sizes, i.e constant size for each model.

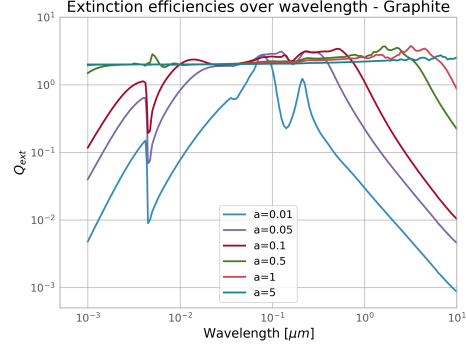
The optical depth of a medium is the logarithm of the ratio between observed to transmitted intensity of light as it has traveled through that medium. It essentially describes how much light passes through a certain medium, and how much light is lost on the way. How the optical depth affects the observed intensity is described by

$$I_{obs}(\lambda) = I_0 e^{-\tau}, \quad (23)$$

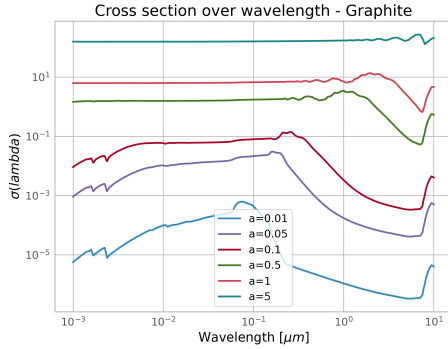
where I_{obs} is the observed intensity and I_0 is the intrinsic intensity of the observed object.



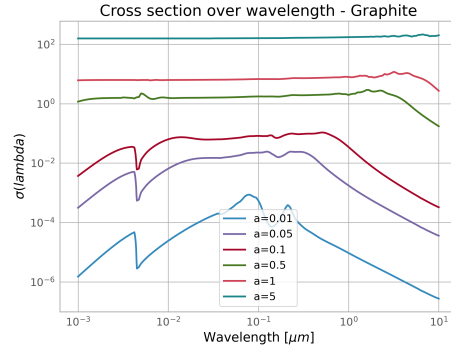
Extinction efficiencies for silicates.



Extinction efficiencies for graphite.



Cross section for silicates.



Cross section for graphite.

Figure 8: Extinction efficiencies ($Q_{extinction} = Q_{scattering} + Q_{absorption}$) for both silicate and graphite for varying dust grain sizes over wavelength. As well as the cross section for both grain materials. Data for the efficiencies are from Laor and Bruce T. Draine 1993

With the optical depth one can also calculate the observed dust attenuated flux F_{obs} of a certain object at a redshift z_{em} observed at a wavelength λ_{obs} using

$$F_{obs}(\lambda_{obs}, z_{em}) = F_{em} \cdot e^{-\tau_{ext}(\lambda_{obs}, z_{em})}, \quad (24)$$

where F_{em} is the intrinsic flux, τ_{ext} is the optical depth due to extinction which can be calculated using Equation 22. This means that the dimming of light emitted at z_{em} and observed at wavelength λ_{obs} can be calculated as (Johansson 2015, Johansson and Mörtzell 2012)

$$\Delta m(\lambda_{obs}, z_{em}) = \frac{2.5}{\ln 10} \tau_{ext}(\lambda_{obs}, z_{em}). \quad (25)$$

6 Using quasars as back light sources

In the previous chapter we discussed the light transmission properties of intergalactic dust. In order to measure these properties from observations we require a well determined back light source enabling us to detect the transmission of its light as it passes through the intergalactic dust. As we will see in the following description quasars are particularly well suited astronomical sources for this task.

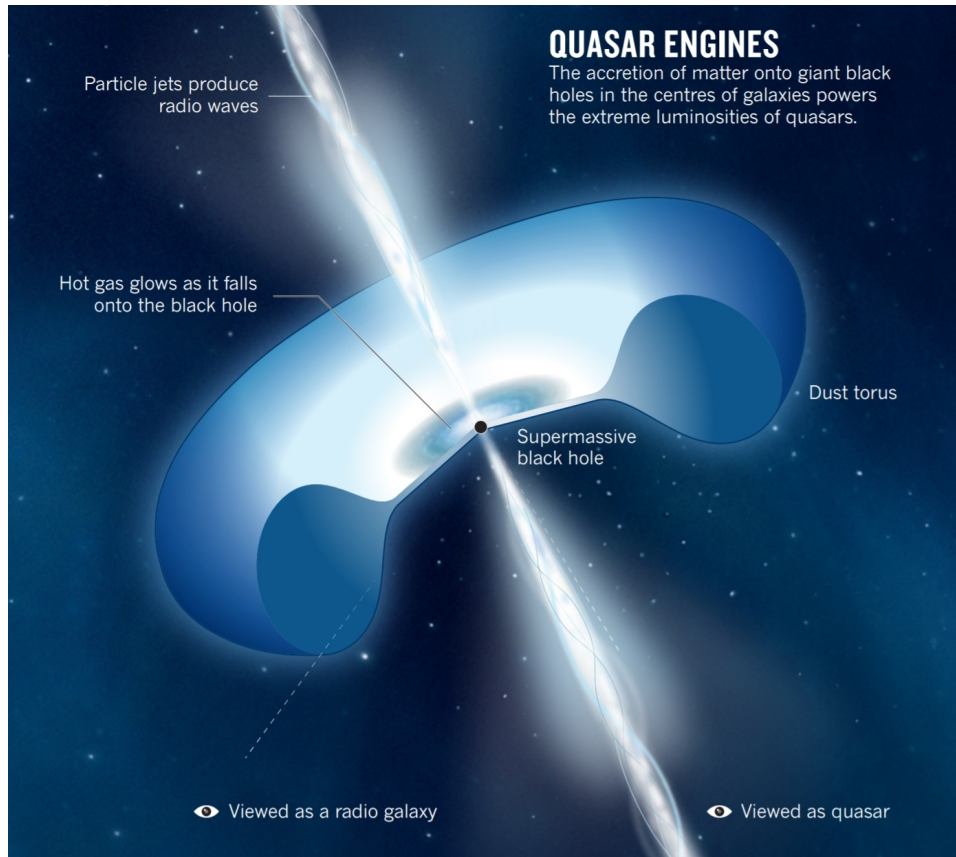


Figure 9: An illustration of an AGN, showing the supermassive black hole in the center with the accretion disc around it. The dust torus that surrounds the black hole is also shown as well as the particle jets. It also shows how the viewing angle change our definition of the object. Image source: Antonucci 2013

6.1 A Quasi-Stellar Object (QSO)

The current state of knowledge says that quasar, or Quasi-Stellar Objects (QSO's), is an extremely luminous type of Active Galactic Nuclei (AGN). AGN's are compact regions in the centers of galaxies with greater than normal luminosities with characteristics indicating that the luminosity is not coming from stars. Sometimes the AGN may be brighter than the entire galaxy it resides in. The leading models suggest that supermassive black holes with masses between $10^7 - 10^{10} M_{\odot}$ reside in the centers of galaxies (Cattaneo et al. 2009; Karttunen H. et al. 2017). Around the black holes there is an accretion disk of gas and dust, and beyond the accretion disk lies a massive dust torus supplying the accretion disk with materials. It is believed that the source of the energy for an AGN comes from the gravitational potential energy of this accretion disk as the gas and dust falls into the black hole. In some cases this may produce jets ejecting matter up to relativistic speeds perpendicular to the rotational plane of the accretion disk. See Figure 9 for an illustration of an AGN.

The conversion of gravitational potential energy into radiation is a more efficient way of converting mass into energy compared to regular fusion in stars. The efficiency ranges from 5.7% for a non-rotating Schwarzschild black hole to 32% for a rapidly rotating Kerr black hole. Comparing this to the efficiency of nuclear fusion of hydrogen of about 0.7% we see

that gravitational energy released by accretion is far superior in its efficiency (Lambourne 2010). Due to the large energy production of AGN galaxies it is unlikely that it will continue through the entire lifespan of the galaxy, and the AGN will eventually quiet down as the mass in the accretion disc is depleted. Thus AGN's are likely not a separate type of galaxies but just a phase that only some galaxies go through before settling as "regular" galaxies (Karttunen H. et al. 2017).

The high luminosity of quasars are believed to be due to the viewing angle of the AGN (Karttunen H. et al. 2017). As seen in Figure 9 if viewed close to the particle jet the AGN will appear as a quasar, in contrast to when viewed from the side through the dust torus when the AGN appears as a radio galaxy. If the particle jet were pointed directly, or almost directly at us the AGN would appear as a strong radio source due to the particles in the jets move at relativistic speeds. These objects are known as blazars (Karttunen H. et al. 2017).

It has been noted that quasars vary greatly in luminosity with time. Sometimes on the range of a couple of days. This means that the quasars generate and emit the light from a small region, since the entire region has to be causally linked on those timescales to incur a coordinated luminosity change. So when observing quasars they appear almost like point sources, which is why they originally were mistaken to be a type of star (Karttunen H. et al. 2017).

Over 750 000 quasars have been observed as of August 2020 (Lyke et al. 2020), most of which has been found by SDSS. It has been shown that quasars were more common in the early universe, i.e towards larger redshifts (Karttunen H. et al. 2017). This might be due to the energy production of quasars not being sustainable on large timescales as well as the universe being more active in the past (see Section 2).

6.2 Properties of QSO's

Quasars are detectable over the entire observable electromagnetic spectrum, from radio to X- and gamma rays. Generally quasars are brightest around their rest-frame ultraviolet wavelength of 1216 Ångströms, which is the Lyman-alpha hydrogen emission line. However many of the observed quasars are at larger redshifts (Lyke et al. 2020) meaning that in the frame of the observer the peak luminosity is often towards larger wavelengths, sometimes even towards the near infrared part of the spectrum (Karttunen H. et al. 2017).

For many quasars their spectra can be described as a featureless continuum in the ultraviolet to optical region with some strong and broad emission lines. When comparing several quasars to each other it has been apparent that most quasars are strikingly similar in terms of their spectra. It has been shown that quasars are similar in terms of both spectral features as well as colours. These similarities even exist over large ranges of magnitudes in their luminosities as well as ranging redshift (Vanden Berk et al. 2001; Telfer et al. 2002; Johansson and Mörtzell 2012). To analyze the difference in emission properties, i.e spectra, studies have looked at differences in the rest equivalent widths of some spectral lines such as $\text{Ly}\alpha$, as well as differences in spectral slope (Peng et al. 1999). The spectral slope is essentially the angle of the slope of the spectrum in a logarithmic coordinate system.

To the extent that quasars are homogeneous in terms of spectra is found in no other astronomical object, which is why quasars are a great object to use as a back light source. Due to the relative homogeneity of quasars one can construct composite template spectra of quasars from a sample of real quasar spectra, i.e an average spectrum (Vanden Berk et al. 2001) (more on this in Section 7.2). Using this composite spectrum one can study general properties of a quasar population, which in our case is the effect of intergalactic dust.

To do that we include this template spectrum in different dust models, where we apply our dust attenuation model to the composite spectrum and compare the results to obser-

vations. We are then able to compare the difference between the result of the model and the real observations for each model. For this thesis we are going to compare the models to observations using colours (more on this in Section 7.5). Due to the homogeneity of quasar colours the difference between the models to observations will be due to differences in the models and not because of differences in the quasars.

To conclude, here are some of the main points why quasars are a good astronomical object to use as our back light source:

- Quasars are relatively homogeneous in terms of both spectral features and colours (Johansson and Mörtzell 2012).
- There are a lot of measurements of quasars over a large span of redshifts (Lyke et al. 2020).
- Quasars are comparable over the entire redshift span (Vanden Berk et al. 2001).
- There exist composite spectra which could be used as the simulated back light source (Vanden Berk et al. 2001; Telfer et al. 2002).

7 Method & Result

This master thesis builds on previous studies of the effects of intergalactic dust. Much of the method is inspired by Johansson and Mörtzell 2012; Mörtzell and Goobar 2003; and Östman and Mörtzell 2005. Below are descriptions of the methods used, thoughts behind each step and the resulting figures. The cosmological parameters of the Planck Collaboration et al. 2020 is used.

7.1 The experimental setup

In this thesis we are interested in the influence of intergalactic dust on observations. To investigate this we construct a forward model of the effects of intergalactic dust on light emitted by quasars following the conceptual outline shown in Figure 10. We construct the model such that we have a simulated distant quasar that emits light into the intergalactic medium where the photons interacts with intergalactic dust grains getting attenuated by dust through scattering and absorption (see Figure 10). How the emitted light interacts with the intergalactic dust is governed by the known equations explained in Section 5.5. We have now modelled our transmitted quasar light and can now compare our model to observations. This comparison will be done using colours, which will later be shown to be optimal for this thesis. If the simulations and real observations agree in terms of the results it means the model is a good representation of real intergalactic dust. And if they do not agree we can tweak the model, like changing the composition or the size of the dust grain sizes. In doing so we are able to constrain the model to fit real observations thus calculating the most probable dust scenarios. In order to do all of this we must first find a way to simulate the quasars as our back light source.

7.2 Simulating quasars as the back light sources

As we saw in Section 6 quasars are a great source to use as our back light source. An additional advantage is that there exist photometric observations for a lot of quasars even towards higher redshifts ($z \sim 3$) which is advantageous since we also want to investigate the redshift dependence of our dust model. Now in order for us to be able to apply our dust attenuation model onto our back light source we need a simulated spectrum for our back

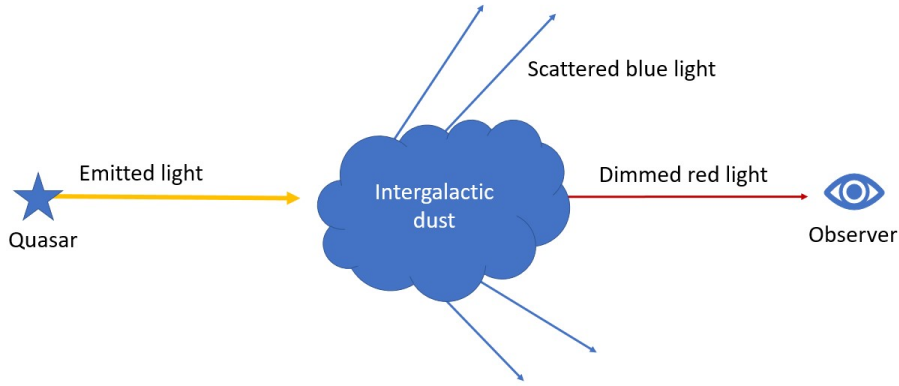


Figure 10: An illustration of the experimental setup of the model. A quasar emitting light through intergalactic dust. As the light travels through the dust it undergoes both scattering and absorption, causing a reddening and dimming of the emitted light as it reaches the observer.

light object. For the simulated spectrum we can use a composite spectrum of quasars. We use the median composite spectrum derived in Vanden Berk et al. 2001, which used over 2200 samples of spectra from SDSS. This composite spectrum spans from 800 to 8555 Å. We splice this spectrum with the composite spectrum produced in Telfer et al. 2002 which used the spectra from 101 quasars observed with the Hubble Space Telescope. This spectrum covered the wavelengths 309 to 3386 Å. The splicing of the spectrum was done to achieve a greater wavelength span of the resulting composite spectrum. We disregarded the part of the spectrum below 342 Å due to the noise and larger errors caused by the Lyman alpha forest. We spliced the spectra at about wavelength 1100 Å to produce the total composite spectra. The resulting composite spectrum can be seen in Figure 11.

7.2.1 The composite spectrum

As previously mentioned in this thesis we will use composite spectrum as our simulated back light source spectrum. A composite spectrum is the mean spectrum from several observed spectra, including as many spectral features of the source as possible. There are a couple of steps to creating a composite spectrum (Vanden Berk et al. 2001):

1. Selecting the input spectra used to generate the composite.
2. Determine accurate redshifts of the spectra.
3. Shifting the spectra to our rest frame.
4. Scaling or normalizing the spectra.
5. Divide the spectra into wavelength bins and calculate the mean spectra for each bin then combine them to generate the complete composite spectrum.

To do this the SDSS composite spectrum (Vanden Berk et al. 2001) used SDSS spectra data for 2204 quasar spanning the redshift range $0.044 \leq z \leq 4.789$ with a median quasar redshift

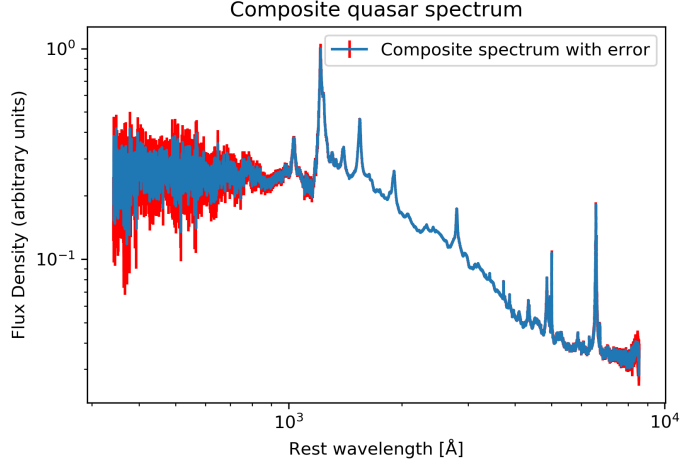


Figure 11: The complete quasar composite spectrum in arbitrary flux units.

of $z = 1.253$. The flux calibration for these spectra used several F subdwarf stars to define the response function. This largely corrects for Galactic extinction. Other steps were also made in the data selection process to minimize the effect of host galaxy extinction (Vanden Berk et al. 2001).

Vanden Berk et al. 2001 created two different composites, the first which preserves the spectral features of the combined quasars, and the second which preserves the global shape of the continuum of the combined quasar spectra. For this thesis we use the first composite which preserves the relative fluxes of the emission features. This is because we are going to be looking at quasar colours, thus the relative fluxes depending on wavelength are important.

In order to determine accurate redshifts Vanden Berk et al. 2001 created a smaller composite spectrum focusing on the [OIII] emission line at wavelength $\lambda 5007 \text{ \AA}$ which could be used as a template. They constructed the composite using 373 QSO spectra with strong [OIII] emissions lines. The wavelength array for each spectra was then shifted to the rest frame based on the position of the [OIII] line and the spectra was rebinned into bins of 1 \AA width in the wavelength space while preserving the flux. The flux density of the bins was then scaled and normalized depending on redshift (Vanden Berk et al. 2001). The final [OIII] composite spectrum was then generated by summing the flux density of each bin for the shifted, rebinned, and scaled spectra. Using the [OIII] composite they were able to more accurately define the redshifts of the spectra missing a strong [OIII]-line or which had the [OIII]-line shifted beyond 9200 \AA . Then the process behind the creation of the [OIII] composite was done again for the complete composite spectrum using all of the 2204 QSO spectra. To create the median composite spectrum preserving relative fluxes they took the median flux density for each bin from the shifted, rebinned and scaled spectra.

The HST composite spectrum (Telfer et al. 2002) is generated in a similar fashion as explained above but using a different data set focused more towards bluer wavelengths. They used 322 HST spectra of 184 QSO's with $z > 0.33$ in order to study ultraviolet spectral properties of QSO's.

A problem with using these composite spectra for our analysis is that of course the spectra used in the generation of the composites might also be attenuated by intergalactic dust.

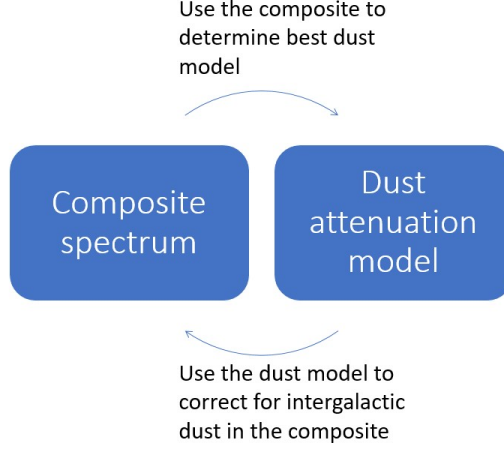


Figure 12: A flowchart showing the iterative correction work that was done to correct for potential intergalactic dust effects in the composite spectrum done in Mörtzell and Goobar 2003

7.2.2 Possible contamination in the generation of the composites

Much has been done in the creation of the composite spectrum to account for Galactic dust extinction and dust extinction from the host galaxy. However there could be cases where the observed spectra they used to generate the composite already are attenuated by intergalactic dust. This is clearly a nuisance since we would prefer the spectrum to be free of dust effects since we are applying a dust attenuation model onto the spectrum.

Mörtzell and Goobar 2003 formed an iterative correction procedure to investigate the influence of possible contamination. They began by using the composite spectrum from Vanden Berk et al. 2001 and using the known dust attenuation equations to guess the dust contribution. Given this guess they were able to correct the original spectrum for the guessed dust contributions. With the new composite spectrum they were able to redo the process of guessing the dust contribution then they iteratively did this entire process until the composite spectrum converged. This process thus reduces the potential effects of intergalactic dust. A flowchart showing this iterative process can be seen in Figure 12.

Now using the final dust-corrected composite spectrum they did the initial analysis again and compared the result with the results from the non-corrected composite. They found that the possible effects from intergalactic dust did not have a sufficiently significant effect on the result in their χ^2 analysis for the result to be invalidated. However this is a systematic effect that is important to take into account. Since their analysis is very similar to ours where we both used quasar colours to analyse intergalactic dust properties with a χ^2 -analysis we also assume these effects would have little influence on our results.

Studying the potential systematic effects in the composite spectra is of great importance in improving the statistics of the result. As will be seen in Section 7.8 the error in the results is governed by the errors in the composite spectrum. Reducing the systematic effects as well as improving the statistics of the quasar surveys should improve the control of these effects when generating the composites and thus improve on the error of the composite.

7.3 Applying dust attenuation to the back light sources

Now we want to apply the dust attenuation, caused by the photons travelling through the intergalactic dust, to the spectrum of the source. For a certain dust model we are now able to firstly redshift the spectra to the redshift we want to look at, then apply the dust attenuation to the flux of the back light source spectra. This is done at each wavelength of the spectrum using Equations 22 and 24. The cross section in the optical depth integral was easily attained from the data from Laor and Bruce T. Draine 1993 for both silicate and graphite, i.e the materials we are assuming our intergalactic dust to consist of. For the comoving number density of dust we used two different models, or approaches.

7.3.1 Constraining the total amount of all dust grains

Initially we just related the comoving number density of dust to the comoving star formation rate, without the inclusion of the n_0 factor from Ω_{dust} (see Section 3.3).

$$n(z) \propto \int_z^\infty dz' \frac{\dot{\rho}_*(z')}{(1+z')\varepsilon(z')}. \quad (26)$$

This is an additional simplification of the model, essentially constraining the total amount of dust grains in the universe to a constant. This is because we have no grain size dependency in this number density, thus changing the grain size of this model does not change to total amount of dust grains. From now on this will be referred to as Model 1. Model 1 was the first model tested since it is an additional simplification of the model, making the model less complex since we have no constrain from Ω_{dust} . It was also made to investigate certain dependencies, for example how would the effect of dust change if all dust grains increased/decreased in size but not change in amount. This could help with checking the validity of the algorithm, seeing if certain steps produce the expected result etc.

Since for this model the comoving number density is invariant under dust size changes it results in $\tau \propto a^2$ due to the only dust size dependency in the optical depth is from the cross section which has a a^2 dependency. This means when looking at how the emitted flux is altered by the dust attenuation (See Equation 24) we see that $F_{obs} \propto e^{-a^2}$. This is quite an unstable dependency on the observed flux since small changes in the dust grain size will cause large changes in the observed flux.

All of the plots produced for Model 1 in the following sections can be seen in Appendix A.

7.3.2 Constraining total mass of all dust grains

The second model included the constrain on the total amount of dust grains from Ω_{dust} by implementing the normalization factor n_0 from Equation 20. Instead of constraining the total amount of dust grain in the universe to a constant this model constrains the total combined mass of all dust grains in the universe. Thus if we increase the size of the dust grains we reduce the total amount of dust grains. This is because of the new dust grain size dependency in the comoving number density, $n \propto a^{-3}$, that comes from the constrain from Ω_{dust} . From now on this will be referred to as Model 28. Model 2 is a more physically appropriate model since putting constraints on the total combined mass of dust grains makes more sense from a scientific perspective as compared to putting constraints on the total amount of dust grains. All of the plots shown in the method and results section will be using Model 2 with $\Omega_{dust} = 5 \times 10^{-6}$ (as given in Ménard et al. 2010).

Since this model has the $n \propto a^{-3}$ dependence in the comoving number density we get the optical depth dependency of $\tau \propto a^{-1}$ since now we have both the dust grain dependency in the cross section, a^2 , and in the comoving number density, a^{-3} , which are multiplied with

each other. This leads to the observed flux being proportional to the dust grain size through $F_{obs} \propto e^{-1/a}$, which is not as sensitive to changes in the dust grain compared to Model 1.

A summary of the features of the two different models is seen in Table 3.

Model features	Model 1	Model 2
What is constant	The amount of dust grains	The total mass of all dust grains
τ dependency on a	$\tau \propto a^2$	$\tau \propto a^{-1}$
F_{obs} dependency on a	$F_{obs} \propto e^{-a^2}$	$F_{obs} \propto e^{-1/a}$

Table 3: A summary of some of the main features and differences of the two models used in this thesis.

7.3.3 Integrating the line-of-sight optical depth of intergalactic dust

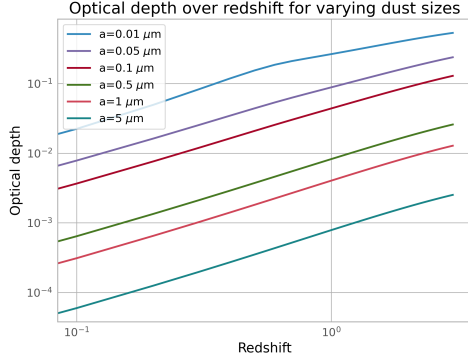
A major part of this thesis has been about making the calculations efficient and not too time consuming. This was especially important when it comes to calculating the optical depth integral (Equation 22) since, as will be discussed later, this integral will be calculated many times over. Even calculating the integral once requires a lot of calculations. This is partly because the comoving number density factor in the integral is itself an integral (Equation 18). This means that at every point during the calculation of the optical depth integral we have to calculate a comoving number density integral.

Because we are going to do a lot of calculations using the optical depth integral the calculation time had to be shortened. One way to do this is to interpolate the parts of the integral. Interpolations was used for the comoving dust density and the cross-section. An issue with using interpolations is that it reduces the accuracy of the calculations somewhat. This depends on how many points we are interpolating. For the cross-section 50 points were used and for the comoving dust density 200 points were used. The reason why we could take 200 points for the dust density will become apparent later on. We still felt that the increase in error was worth the reduced computation time since the computation time got reduced by a factor of 100 and the numerical error from the integral calculation went from a 0.000113% to 0.0024%. Note that this is not the total error, but only the error from the integral calculation. In Figure 13 we see the result of the optical depth integral ranging over redshifts in the range $0 < z < 3$. The first plot is for varying dust grain sizes, and the second is for varying wavelengths. Both of the plots are for silicates.

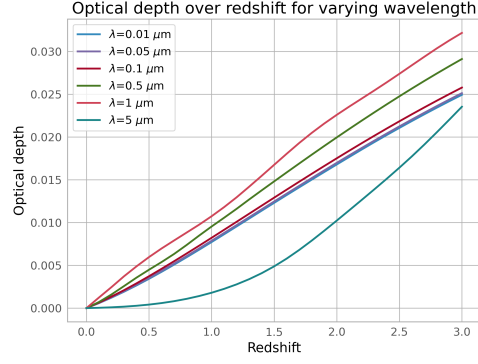
7.3.4 Predicting dust attenuated quasar spectrum

According to the forward model described in Section 7.1, we will use the composite spectrum to estimate the emitted flux of a quasar at redshift z . To do this we first redshift the spectrum to the quasar's restframe. This is done by multiplying the wavelengths by $1+z$ then at each redshifted wavelength of the composite spectrum we multiply the flux with $e^{-\tau_{ext}(\lambda_{obs}, z_{em})}$ where $\tau_{ext}(\lambda_{obs}, z_{em})$ is from Equation 22. Practically this is done using interpolations. The optical depth is calculated for the redshifted wavelength array of length 50, equally spaced, covering the entire span of the redshifted spectrum. Since the optical depth's dependence on wavelength is rather smooth using interpolation does not incur that great of an error. This means that for each spectrum we want to attenuate we have to calculate the optical depth integral 50 times, once for each wavelength bin.

We see how the optical depth changes over wavelength for both varying dust sizes and redshifts for silicates in Figure 14. Now that we have $\tau_{ext}(\lambda_{obs}, z_{em})$ we can then apply the dust attenuation on to the entire composite spectrum to produce our simulated dust

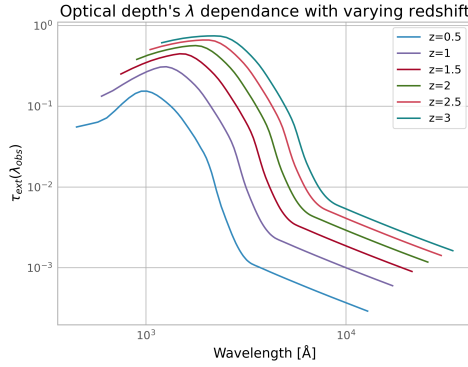


Constant wavelength, $\lambda = 0.1 \mu\text{m}$

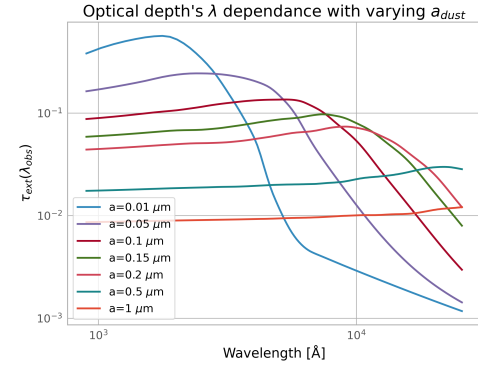


Constant dust size, $a = 0.1 \mu\text{m}$

Figure 13: The optical depth as a function of redshift, $\tau(z)$. First plot with constant wavelength and varying dust size and the second plot with constant dust size and varying wavelength. Here we note increasing optical depth with increasing redshift, as well as with decreasing dust grain size.



Constant dust size, $a = 0.01 \mu\text{m}$



Constant redshift, $z = 2$

Figure 14: The optical depth as a function of wavelength, $\tau(\lambda_{obs})$ for constant dust grain size (left figure) and with constant redshift (right figure). As seen in the left figure with increasing redshift the optical depth increase as expected since the light has to travel through more dust. The the shape of the curves in the right figure is caused by the extinction efficiency which differ for different dust grain sizes. Generally we have larger dust attenuation towards lower wavelengths.

attenuated spectrum. In Figure 15 we can see a couple of spectra which has been affected by dust attenuation with different dust sizes or redshifts for silicate dust grains.

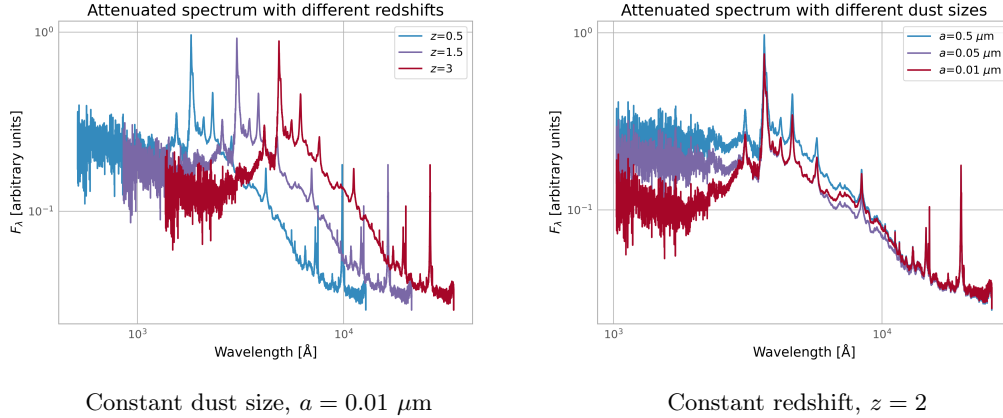


Figure 15: The predicted intergalactic dust attenuated spectra of back light sources with a constant dust grain size of $a = 0.01 \mu\text{m}$ with changing redshift (left figure) and with constant redshift $z = 2$ with changing dust grain size (right figure). Both are for silicates. In the left figure we see the spectra are shifted in the wavelength span due to their redshifts, as well as the fluxes being attenuated more towards larger redshifts at lower wavelengths. In the right figure we see larger dust attenuation for smaller dust grain sizes towards lower wavelengths. This is caused by the dependencies shown in Figure 14

7.4 Discussion of the dust attenuation model

Now lets discuss the the application of the intergalactic dust attenuation through the optical depth integral. We start by looking at the comoving number density.

7.4.1 The distribution and number density of intergalactic dust

For the number density we used two different models (see Sections 7.3.1 and 7.3.2). We choose to use Model 2 throughout this thesis (except for Section 7.6) since it is more plausible for the number density of dust to be correlated to the total amount of dust.

Model 2 has the constrain that with changing dust grain size we set a constant mass density of dust grains in the universe, Ω_{dust} . This creates a relation between the dust grain size and the amount of dust grains. Increasing the dust size decreases the amount of dust grains. Ω_{dust} is something we can constrain by observations, while if we look at Model 1 where with changing dust grain size we constrain the total amount of dust grains to be a constant. Here as we increase the dust grain size the total amount of dust grains will remain the same, resulting in the amount of dust in mass units increase. Essentially here we have a constant total amount of dust grains, which would make little sense it if were independent on dust grain size. It is also more difficult to constrain the amount dust grains, independent on size, through observations. Since what actually causes the effects from dust depends on the mass density of the dust grains, and not strictly the amount.

For both of the models we assume that intergalactic dust is produced by stars and expelled from their galaxies. To do this we assume that the number density of dust follows the star formation rate given in Hernquist and Springel 2003. However this is a slight simplification since not all of the dust is created during the formation of stars. Instead they are created during later stages of their evolution (see Section 2. Another simplification we make for the number density of dust is that we assume the distribution of intergalactic dust to be isotropic, i.e the same in all directions, which is not strictly true. Since intergalactic dust

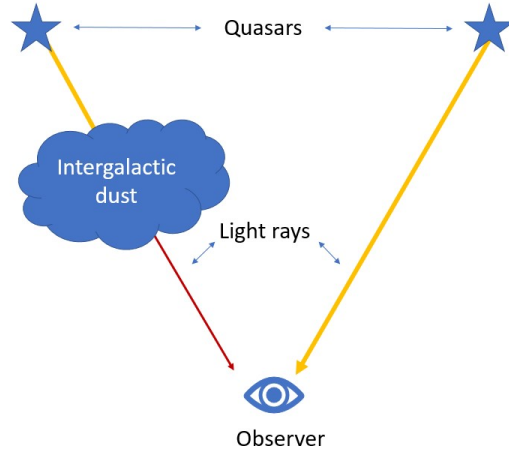


Figure 16: A conceptual image showing the possibilities of different quasars being more or less influenced by intergalactic dust compared to others. These differences depends on the spatial distribution of intergalactic dust. For the quasar emitting light through intergalactic dust we see the light gets both reddened and dimmed, compared to the light from the un-attenuated quasar.

spawns from galaxies we expect higher concentrations of dust around galaxies and galaxies are not evenly distributed in space (Barbara Ryden 2006a). We would thus expect higher number densities of dust towards regions with more galaxies compared to regions with less galaxies. This means that not all quasar spectra at equal distance are affected equally by intergalactic dust. Some quasar light may travel through denser dust regions compared to others, as depicted in Figure 16. One could take advantage of this fact when generating composite spectra to reduce the systematic errors from by possible contaminations from intergalactic dust. To do this one could generate a intergalactic dust distribution map from the distribution of galaxies, then choose spectra from quasars which are in line of sights with relatively low amounts of dust to generate the composite. Another way to produce a cleaner composite spectrum would be to create a composite spectrum from quasar observations at lower redshifts. Since the further away the object is the more intergalactic dust the light will encounter on its way to us. By reducing the distance of light travel it would also reduce the effects from intergalactic dust and thus reduce the systematic errors (Östman and Mörtzell 2005).

Taking into account the spatial distribution of dust one could also produce more accurate dust models since we would have more accurate numberdensities of dust when we compare the models to real observations. We could also use this to more accurately correct for the effects intergalactic dust have on observations when taking into account how much dust is in the line of sight of each observation. The inhomogeneity of the dust distribution was something this thesis originally aimed at analysing, however other parts of the thesis took over and creating the algorithms took longer than expected.

Assuming a homogeneous distribution of dust likely does not incur that great of an error, since we essentially take the average of all directions and use observations from all directions. However with increasing precision of measurements such small systematic errors, as assuming a homogeneous dust distribution, may become of larger importance. We see in Figure 7 the comoving number density of dust using the star formation rate in Hernquist

and Springel 2003. Here we notice the increase in number density towards lower redshifts, which is expected since the intergalactic medium is continuously enriched by dust through various processes.

7.4.2 The properties of dust, their structure and cross section

When it comes to the actual intergalactic dust grains several simplifications were made. Firstly for our model we only assume either silicate or graphite, while in reality it is likely a mixture of them both with some smaller contributions from other materials (B. T. Draine 2003a). We also assume only spherical dust grains with the same dust grain size for the entire dust population. The data used for the interaction efficiencies are also from laboratory measurements and not astronomical measurements (Laor and Bruce T. Draine 1993). In the end I believe the assumptions made are valid and the same assumptions are made in several previous studies. It has been shown that a composition of spherical grains of either silicate or graphite make up for a valid dust model (Johansson and Mörtzell 2012).

7.4.3 The dependency of optical depth on model parameters

Now we come to the result of the optical depth integral. As seen in figure 13 we see the evolution of the optical depth over redshift for varying grain sizes and wavelengths. We see the general trend of the optical depth increasing with redshift, which is expected. We also see that the optical depth increase with decreasing grain size, as expected considering the $\tau \propto a^{-1}$ dependency of the optical depth for Model 2 (see Section 7.3.2).

We can now take a look at how the optical depth evolves over wavelength which is important since it determines how the optical depth is applied to the composite spectrum (see Section 7.3.4 which we will discuss in the next section). In Figure 14 we can see the evolution of optical depth over wavelength. In the left figure we see the same redshift dependency as discussed above, with increasing redshift the optical depth increases. In the right figure we see that the evolution of optical depth is highly dependant on the dust grain size. This is because the only wavelength dependency we have in the optical depth comes from the extinction efficiency, which is also highly dependant on dust grain size as seen in Figure 8. The shape of the optical depth curve in these plots is thus caused by shape of the extinction efficiencies. This is further supported by the tests done in Section 7.6 where we concluded that the only wavelength dependency in the optical depth comes from the extinction efficiency.

7.4.4 Dust attenuated quasar spectra

We can now discuss the predicted dust attenuated spectra, where we applied our dust attenuation model onto the composite spectra. Here we essentially just multiplied the redshifted composite spectra with $e^{\tau_{ext}(z, \lambda)}$ where $\tau_{ext}(z, \lambda)$ is the functions shown in Figure 14. We see the result of this in Figure 15, where we see with varying redshifts firstly we see the shift of the spectrum across the wavelength axis caused by the redshift. We also see that the the lower wavelength portion of the spectra gets more attenuated with increasing redshift. This is because the optical depth peaks towards lower wavelengths for this grain size and the optical depth increases with redshift. In the second figure we see that with lower dust grain size it leads to increasing attenuation. All of this behaviour is explained by the optical depth wavelength dependency explained above.

7.5 Comparing predictions to observed quasar colours

As illustrated in Figure 10 we are now able to predict the attenuated quasar spectra. To compare these model predictions to observations we will be using colours. This is advanta-

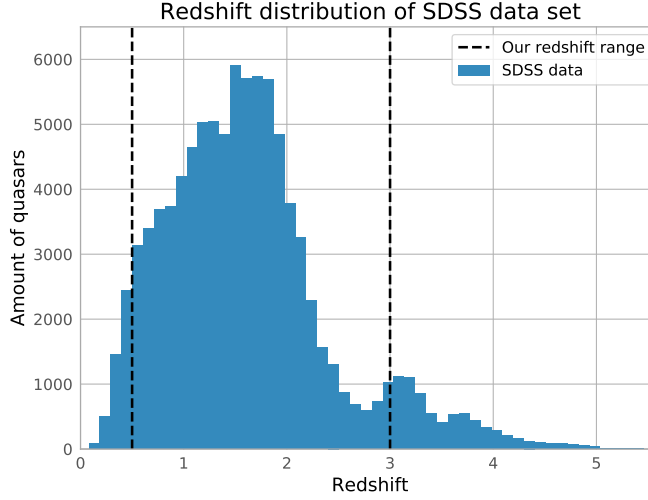


Figure 17: The redshift distribution of the quasars in SDSS DR7. Here we see that we have a larger amount of quasars in the redshift range 0-2, hence we will have a larger statistical significance from this redshift range.

geous since there are a lot of photometric measurements of quasars publicly available (Lyke et al. 2020). Additionally since colours are the difference in magnitudes for different filters (see Section 4) it is essentially a logarithmic difference between fluxes. This means that any systematic effect or factor that is multiplied evenly over the entire spectrum cancels (see Equation 14). Also note since our simulated spectrum is in arbitrary flux units by using colours such normalization factors will cancel.

7.5.1 Observed quasar colours

We will use data from SDSS’s Data Release 7 (DR7) (Schneider et al. 2010), which contains 105783 confirmed QSO’s with magnitudes in the five SDSS filters (u, g, r, i, z). Only QSO’s with magnitudes over $[u, g, r, i, z] = [22.3, 22.6, 22.7, 22.4, 20.5]$ is considered, corresponding to a S/N ratio greater than 5:1 to avoid quasars with too much noise (Richards et al. 2001). This cuts the data down to 97153 QSO’s. Quasars which are classified as extended sources are also disregarded to minimise the contamination from host galaxies. What is left is 93305 point sources with sufficient S/N ratio. We also only look in the redshift range $0.5 \leq z \leq 3$ since that is the range with the most amount of quasars in the data, resulting in the greatest statistical significance. Also below $z = 0.5$ the data is more likely to contain Seyfert galaxies and the quasar spectra at these redshifts may be contaminated by their host galaxies (Mörtsell and Goobar 2003; Östman and Mörtsell 2005). The redshift distribution of the SDSS quasars is shown in Figure 17.

To get the colours from the real observations we divide the observations into redshift bins of size $\Delta z = 0.05$ in the redshift range $0.5 \leq z \leq 3$. For each bin we calculate, for every filter X and Y , the average colour $(X - Y)_z^{obs}$ for all of the observed quasars in that bin. Quasars that diverge more than 2σ from the average colour are rejected to remove contaminations from anomalous colours, for example from quasars which has extensive extinction from their host galaxy (Mörtsell and Goobar 2003). The SDSS flux calibration should take much of these effects into account but outliers always exist (Masataka Fukugita 2011).

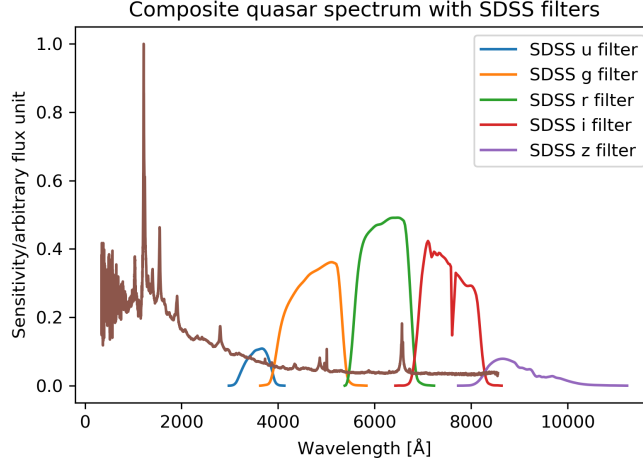


Figure 18: The SDSS filter transmission functions superimposed on the composite spectra. This shows which part of the spectra is covered by the filter functions. As the spectra is redshifted the spectra will move to the right in the plot, changing which sections of the spectra are covered by a certain filter.

However the spectrum blueward of the Lyman- α ($\text{Ly}\alpha$) emission line are heavily affected by absorption due to the $\text{Ly}\alpha$ forest, thus decreasing the flux from those wavelengths (Vanden Berk et al. 2001). This is apparent when looking at Figure 11 where the error is greatly increased blueward of the $\text{Ly}\alpha$ line. That means at higher redshifts the bluer filters will extend into this region making the filters inefficient for those redshifts. To address this we only include QSO's with $z < 1.5$ for the u -filter and $z < 2.3$ for the g -filter (Johansson and Mörtzell 2012). Now we have all 10 different colours for each redshift bin, the result of this can be seen in Figure 19.

7.5.2 Predicted quasar colours

For the simulated colours we also divide them in the same redshift bins. Then we specify the dust grain material and size. For each redshift bin we create a dust attenuated spectrum following the steps in Section 7.3. For each redshift bin we then apply the SDSS filter functions to the spectrum for that bin to get the simulated fluxes in the SDSS filters.

We apply the filter functions on the simulated spectrum as:

$$f_x = \int f_\lambda \cdot T_F(\lambda) d\lambda \quad (27)$$

where f_x is the filter flux for the filter x , f_λ is the composite spectrum flux density and $T_F(\lambda)$ is the filter sensitivity depending on wavelength. In Figure 18 we can see the filter transmission curves along with the composite spectrum.

Practically we compute the filter fluxes using the python package Pyphot (*Pyphot*, M. Fouesneau 2016). Pyphot is equipped with tools to calculate and filter flux, and is able to account for scenarios where the filter functions extends beyond the available spectrum (as can be seen in Figure 18 for the z filter). Once we have the filter fluxes we can easily convert these into colours. Again we only calculate colours with the u -filter for bins with $z < 1.5$, and the g -filter for bins with $z < 2.3$ as explained in the previous section. In Figure 20 we see the colours for silicates, the left figure shows all colours for $a = 0.1$ and the right figure shows the $i - z$ colour for several dust sizes.

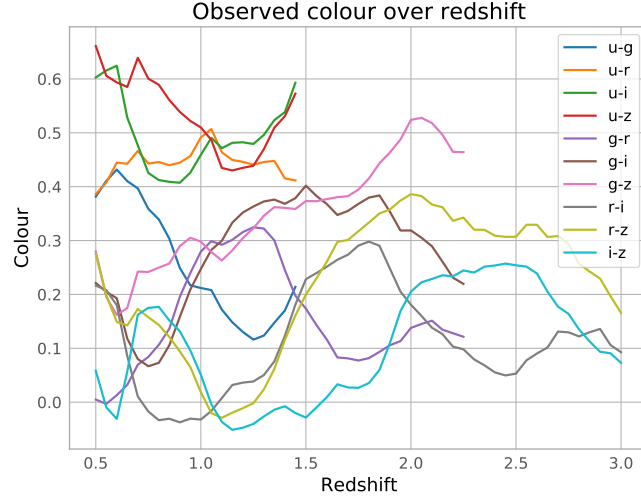


Figure 19: The evolution of the 10 SDSS colours for observations at different redshifts. Here we see how the colours change as the quasar spectra gets redshifted, which results in the filter functions covering different parts of the spectrum as it gets redshifted (see Figure 18). These will later be compared to the expected colours from the model simulations.

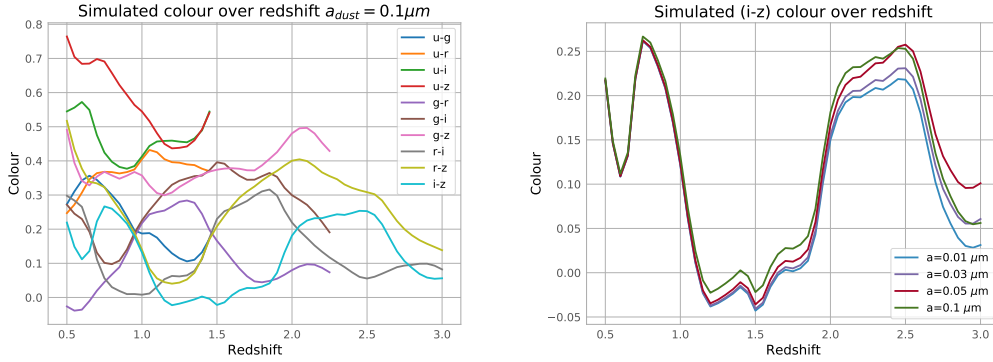


Figure 20: The colour evolution over redshift. All of the colours for a dust model with $a = 0.1 \mu\text{m}$ (left) and the (i-z) colour for models with several different dust sizes (right). We see that the shape and magnitude of the left figure colours resembles the observed colours of Figure 19. We also see slight differences in the (i-z) colour between different dust sizes in the right figure, especially towards larger redshifts.

7.5.3 Comparing simulations to observations

Now that we have all of the colours for both the simulations and the real observed colours we can start to compare them. We do this using the following equation

$$\Delta(X - Y)_z = (X - Y)_z^{obs} - (X - Y)_z^{sim}, \quad (28)$$

where $(X - Y)_z^{obs}$ is the observed colour and $(X - Y)_z^{sim}$ is the simulated colour for the filters X and Y . This equation will be utilized in the coming section about the statistical analysis

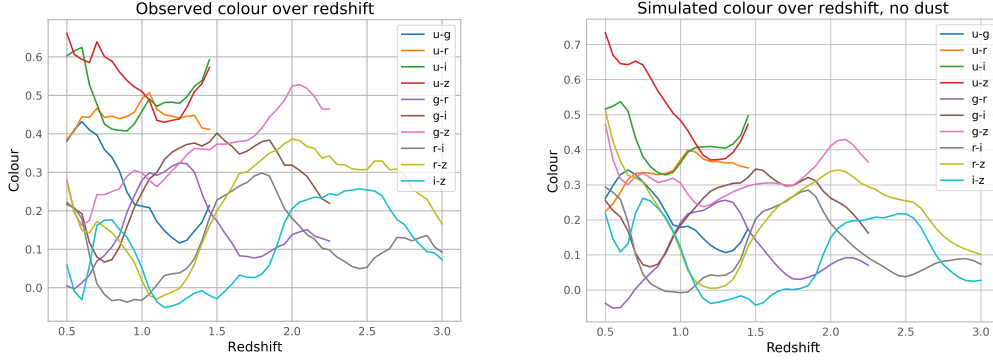


Figure 21: Side by side comparison of the observed colours and the colours from the composite spectrum without the dust model applied to the spectrum. Here we see the colours are fairly similar both in terms of shape and magnitude, which is expected since they are both the quasar colours.

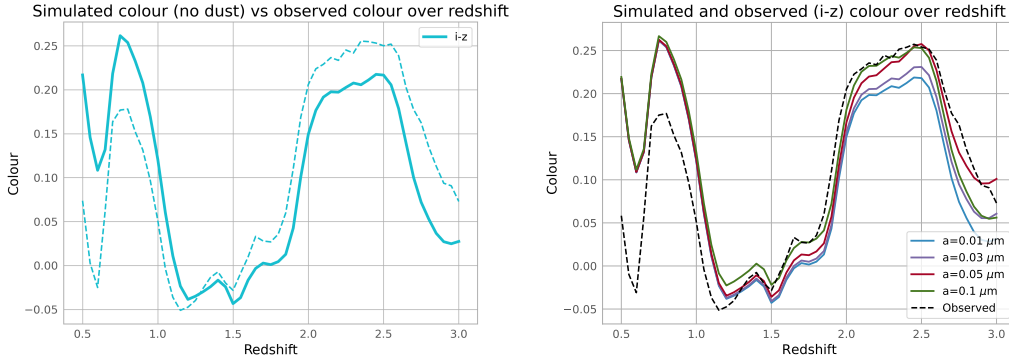


Figure 22: The colour evolution over redshift for the (i-z) colour. The left figure shows the observed colours (dashed) and the colours of the composite spectrum without the dust model applied to it (full). The right figure shows the colour for a couple of different dust models being applied to the composite spectrum, as well as the observed colour.

of different dust models. In Figures 21, 22 and 23 a couple of plots can be seen showing different colours and comparing simulated colours to observed colours.

As can be seen in Figures 22 and 23 below about redshift $z = 1.3$ we see that the observed colours are bluer compared to the simulated colours. This is an error in the analysis. Due to this offset any dust attenuation applied to the simulated colours below this redshift will lead to a negative correction since dust attenuation leads to reddening. This is likely an error caused by the composite spectrum. As explained in Section 7.2.2 there are possible contaminations from intergalactic dust, as well as other sources of errors. These effects could lead to this offset, possibly producing a bias in the result. As will later be seen in Section 7.8 the error from the composite spectrum is the leading error in the analysis, i.e reducing the errors in the composite spectrum is of great importance to improve on the result.

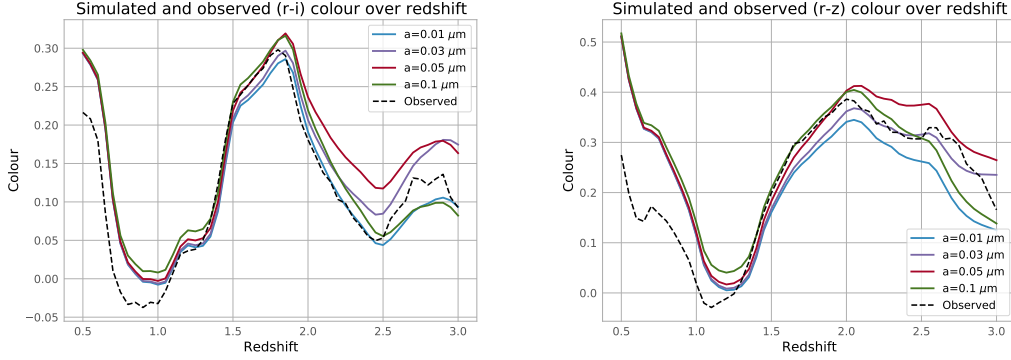


Figure 23: The colour evolution over redshift for the (r-i) and (r-z) colours. The figures shows the colour for a couple of different dust models being applied to the composite spectrum, as well as the observed colour.

7.6 Testing colour calculations with varying degree of complexity

We tested the implementation of the quasar colour calculation by using different spectra which had varying degrees of complexity in the dust model which were applied to them. We then calculated the colours of the spectra and analysed the result. These spectra are as following:

1. A baseline spectrum with constant flux, basically a horizontal line.
2. The composite spectrum, without any dust attenuation at all.
3. The composite spectrum with dust attenuation but with constant interaction efficiency, leading to a constant cross section for a certain dust grain size.
4. The composite spectrum with changing sigma, the model we are looking into.

We chose these different test scenarios to highlight different aspects of the physics model. The aim of this section is essentially to investigate the colour analysis and see if it agrees with theories and equations. This is useful in the search for errors in the calculations, which would be found if the actual results would differ from the expectations from theory. For example we want to test that the shape of the colour curve comes from the change in flux over the spectrum, that the wavelength dependency in the optical depth comes from the extinction efficiencies etc. We do this by starting from a very simplified model, the baseline spectrum, which is not a real physical model but just constructed for testing purposes. Then add complexity, like using the composite spectrum or adding the dust attenuation model. For each successive step we analyse the results to see whether the produced results agree or not with the expectations, and if the results make sense in the context of what we are doing. For these tests the model which assumes a constant amount of dust grains was used (e.g Model 1, see Section 7.3.1) since this model produces the most significant changes in colours depending on the dust size. Note that this is the only section using this model. All of the plots are for silicates and at redshift $z = 2$. Below we further explain each spectrum as well as the results from the colour calculations.

7.6.1 1. Baseline spectrum

We assume the spectrum to just be constant over wavelength, which also means the spectrum is invariant under redshift. Thus the colour we calculate will stay the same indifferent of

redshift resulting in constant horizontal lines in the colour over redshift plot, which is exactly what we see in Figure 24. This is not a physical model, just used to test the technical implementation of the colour calculations.

7.6.2 2. Composite spectrum with no dust attenuation

To understand the impact of the spectral features, we use the composite spectrum without any dust model applied to it, as described in Section 7.2.1. This means that the colour calculations will vary over redshift as the spectrum is no longer constant over wavelength, meaning as we shift the spectrum in the wavelength dimension the colours will change as the flux changes. Thus we expect the colour calculation of the quasar composite spectrum to closely resemble the observed quasar colours from SDSS, which is what we see in Figures 24 and 22(left) where both the magnitude and shape of the colour curve resembles the observed. This is a good confirmation that at least part of the colour calculation and its application on to the composite spectra are correct.

7.6.3 3. Composite spectrum with dust attenuation with constant cross-section

As a next step we introduce our dust attenuation model, but for simplicity we first set the interaction efficiency to a constant. This results in a constant cross-section since we calculate for a certain dust grain size ($a = 0.1 \mu\text{m}$). Thus we remove the wavelength dependence from the optical depth (equation 22) and our model which results in the dust attenuation just being a constant which is applied equally to the entire spectrum. When we calculate the colours, which is a logarithmic difference between parts of the spectrum, this constant will get removed (see Equation 14). The result from this should be that the colours are identical to the case where we have no dust attenuation, which is exactly what is seen in Figure 24, where the colours perfectly overlap. If they would not overlap it would mean we had some wavelength dependence in our optical depth outside of the cross section, which we should not have. Yet another promising result.

7.6.4 4. Composite spectrum with dust attenuation

Finally we use the full dust model which has a wavelength dependence. Here we are calculating the colours for two different dust grain sizes. Generally for larger optical depth we are expecting the colours to be further reddened by the intergalactic dust, e.g the colours are larger for a larger optical depth. A general feature of the model we are looking at in this section (Model 1) is that with increasing dust grain size the optical depth will increase (see Figure 27). This is because we assume a constant amount of dust grains, thus with increasing dust grain size we will effectively get more dust in the universe (in mass units). The result of this is that larger grain sizes will lead to larger colours. Another thing affecting the result of the colour calculation is how the optical depth changes over redshift. Since the light from the object has to travel through more dust the further away it is the optical depth increases with redshift (again see Figure 27). These features lead to us expecting the dust attenuated colours to be slightly (or not so slightly depending on dust size) larger than the colours from the composite spectrum, with the reddening increasing towards larger redshifts. This is exactly what we see in Figure 24 where the spectra with our dust model are more reddened, with larger reddening for larger dust grain sizes. Again a good confirmation that the colour calculations work and does what we expect when we apply our dust model.

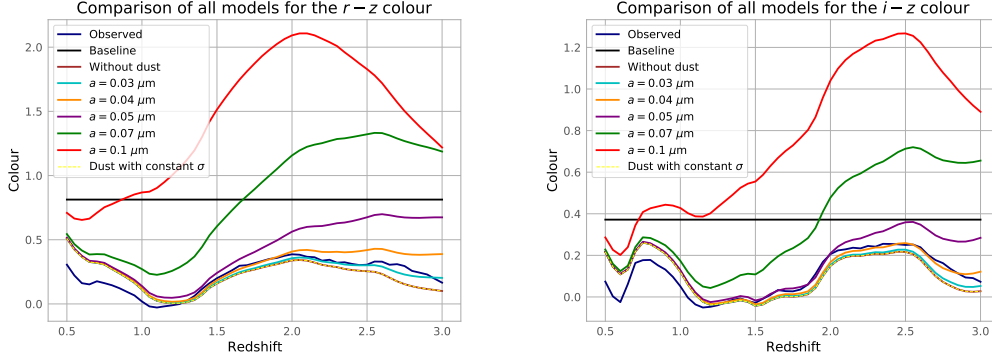


Figure 24: Comparing models with different complexity against observations using the colours $r-z$ (left) and $i-z$ (right). We see the baseline as a horizontal line, the spectra without dust and the one with constant σ overlaps, and the spectra with grain sizes has increased reddening with larger grain sizes. We also see the spectra with $a = 0.05 \mu\text{m}$ are comparable to the observed colours.

7.6.5 Conclusion from the testing

The results from the tests of the different models with varying complexity confirms that the model correctly accounts for the relevant effects. The results shows:

- The colour calculation depends on the changing flux over wavelength of the spectrum, as expected.
- The colours of the composite spectrum matches the observed SDSS colours in both shape and magnitude.
- Our only wavelength dependency in the dust model comes from the extinction efficiency from the cross section, as it should.
- Applying the dust model from Model 1 to the composite spectrum reddens the colours, with further reddening for larger dust grain sizes and towards larger redshifts.

7.7 Discussion of colour comparison

Now lets look at the results of the colour analysis. The shape of the colour vs redshift plots are caused by the shift of the spectrum along the wavelength axis as the quasar is redshifted. Since the wavelength span of the filter functions is set, as the quasar spectra are redshifted different part of the spectra will move in and out of the filter functions. This then leads to the magnitudes, and consequently the colours, changing over redshift. For example the spectra might peak in one particular filter for a particular redshift. But as the spectra is shifted towards different wavelengths the peak may move into the wavelength span of different filter functions.

In Figure 20 we see all of the simulated colours and the simulated $(i-z)$ colour for a couple of different dust sizes. In the right figure we see that the colour varies slightly for each different dust grain size. This is because of the different wavelength dependency in the optical depth for different dust grain sizes as seen in the right figure in Figure 14. The dust grain size that leads to the most dust attenuation, i.e largest optical depth, over a certain filter will cause the most reddening and thus have the largest colour.

We can now look at the comparison between the observed and simulated colours. In Figure 21 we see a side by side comparison of the observed colours vs the simulated colours for only the composite spectrum, without our dust model applied to it. We see that the shape of the colour curve matches fairly well. Then in Figures 22 and 23 we see a comparison of the (i-z), (r-i) and (r-z) colours. In Figure 22 we firstly see the simulated composite colours and the observed colours compared to each other in the left figure, and in the right we compare the observed and simulated colour for different dust grain size models.

We see that certain dust size models produce colours that better match the observed colours than others. This is what we look at to determine which dust size model is the best fit to the real observations. As previously discussed we also see that all of the simulated colours are always more reddened towards lower redshifts below about $z = 1.2$. This points toward some possible systematic error in the composite spectrum towards lower redshifts. It might be an offset created by the effects of intergalactic dust on the generation of the composite (see Section 7.2.2). This offset might cause a bias in the results and to produce more definitive results improvements are needed taking into account or removing the systematic effects in the composite spectrum.

7.8 Analyzing parameters to fit simulations to observations

We are now ready to look at different dust models, i.e different dust grain sizes and composition, and see how they compare to observations. We do this by performing a Pearson's χ^2 test (Pearson 1900). Essentially what we do is calculating the square difference between all of the observed and simulated colours for each redshift bin for each dust model. This is done by the following χ^2 equation (Johansson and Mörtzell 2012):

$$\chi^2 = \sum_{i,j=1}^N \Delta(X - Y)_i V_{i,j}^{-1} \Delta(X - Y)_j, \quad (29)$$

where N is the total number of redshift bins, and i and j are the different bins. $V_{i,j}$ is the covariance matrix and

$$V_{i,j} = \sigma_{cali}^2 + \sigma_{comp}^2 + \delta_{ij} \sigma_{obs}^2, \quad (30)$$

where σ_{cali} is the calibration uncertainty of the photometric system and is given as ~ 0.02 (M. Fukugita et al. 1996). σ_{comp} is the uncertainty of the power-law fits to the composite spectrum and is given as ~ 0.10 in Vanden Berk et al. 2001, and lastly σ_{obs} is the uncertainty of the SDSS DR7 colours and is given to be ~ 0.003 in Schneider et al. 2010.

The idea for this statistical analysis is that the dust model which best fits to the observations would produce the smallest χ^2 . Hence we can look at χ^2 to determine how good the different models fit the observations and thus constrain what are the more likely dust sizes for each dust composition. In Figure 25 we see the result from this analysis for both silicate and graphite for dust models with $\Omega_{dust} = 5 \times 10^{-6}$. For these dust models the results favors dust grains around size $a = 0.05 \mu\text{m}$ for graphite and $a = 0.08 \mu\text{m}$ for silicate. Also silicate produces a smaller χ^2 meaning that silicate produces the better fit to observations.

We also performed a 2d grid search for both the grain size and Ω_{dust} for each dust model for silicate. The result of this can be seen in Figure 26 which shows the logarithmic value of the χ^2 as the colour with smaller values being darker, i.e the darker the colour the better the fit to observations. This calculation show a favor for dust grain sizes around $a = 0.08 \mu\text{m}$ and Ω_{dust} around $5 - 7 \times 10^{-6}$. This result is in agreement with previous estimates (Johansson and Mörtzell 2012).

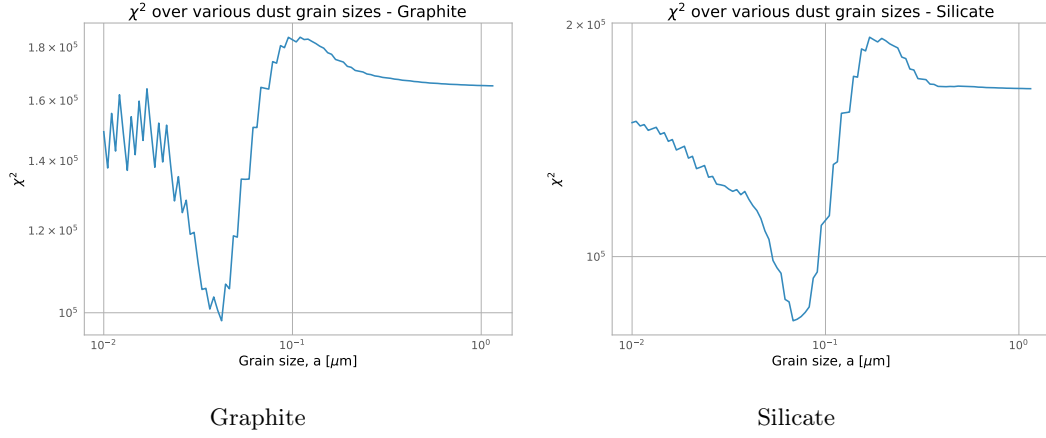


Figure 25: The results from the χ^2 calculations for both graphite and silicate. This is a measure of how closely the dust model matches observations where the smaller χ^2 the better that model fits to observations. This means that the grain size that produces the minimum in χ^2 is the dust size that produces the colours that is the closest to the observed data. The reason behind the "step-like" curve is the extinction efficiency data. This data is only available for certain dust sizes leading to the "step-like" shape.

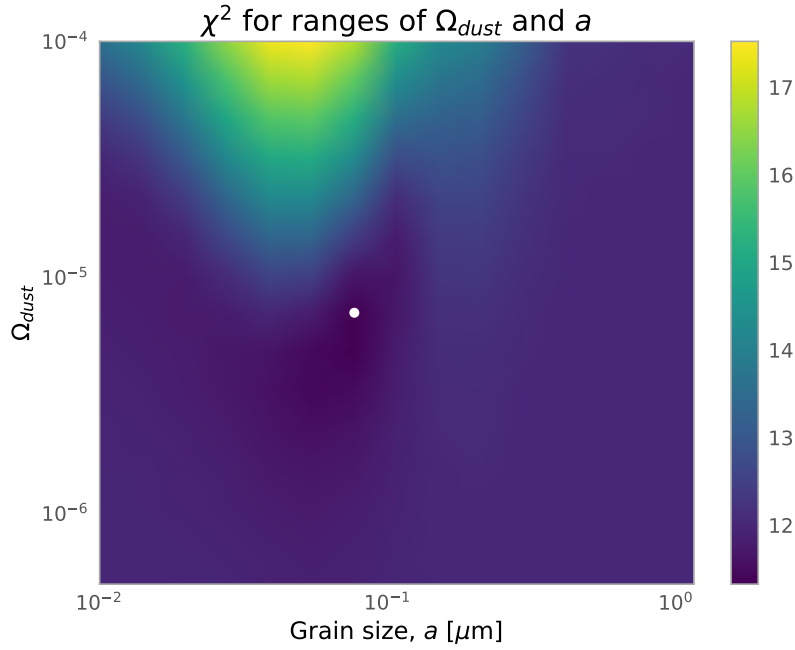


Figure 26: The two dimensional colour plot calculation spanning over both Ω_{dust} and the dust grain size for silicate. The colour shows the logarithmic χ^2 value for that grid, i.e the darker the colour the more probable the dust model is and the minimum is marked with a white dot. The colour bar shows the logarithmic χ^2 value.

8 Discussion of the statistical analysis and findings

Now we come to the statistical analysis part of this thesis. Here we compute, for each dust mode, the total difference between the simulated and observed colours for all of the colours for all of the bins and sum them up. This was done for several dust models with varying dust grain size, composition and Ω_{dust} . The model that produces the smallest difference is then the model that is best fitted to the observations and the dust model that best represents real intergalactic dust. In this process we take into account the errors from the composite spectrum, the colour calculations and the error in the observed data. As seen in Section 7.8 the combined error of this calculation is determined by the error of the composite spectrum, and the error from the observed data and the colour calculations are comparably insignificant. This means we must first reduce the errors in the composite spectrum before reducing the other errors would contribute to significant reductions in the total error. Thus using a newer data set with improved errors would not contribute much in the improvement of the results. To produce more definitive results improvements of the composite spectrum are required, specifically taking into account or removing systematic effects such as the possible effect of intergalactic dust in the composite spectrum.

The result of the statistical analysis suggests that a dust model with $\Omega_{dust} = 5 \times 10^{-6}$ favors dust grains around size $a = 0.05 \mu\text{m}$ for graphite and $a = 0.08 \mu\text{m}$ for silicate. Both of these results are within the limits given in Johansson and Mörtzell 2012, with the graphite size being just above the lower limit. This analysis also suggests that dust models with silicates are favored, as the χ^2 was smaller for silicate compare to graphite. When the statistical analysis was done over both ranging dust sizes and Ω_{dust} the results suggests that dust models with the same dust sizes as mentioned above with a Ω_{dust} around $5 - 7 \times 10^{-6}$ are favored. This is also in rough agreement with previous estimates of Ω_{dust} (Masataka Fukugita 2011; Johansson and Mörtzell 2012). This shows that intergalactic dust exist, and has a notable effect on cosmological measurements and favors dust grains consisting of silicate with a size around $0.1 \mu\text{m}$.

9 Conclusion & summary

In the current cosmological paradigm we have a universe which is expanding at an accelerated rate. This expansion is supported by the observations of Type Ia supernovae. However in order to get accurate measurements one has to take into account the systematic effects and errors that may influence the observations. The reddening and dimming caused by the interaction between the light emitted by the supernovae and the intergalactic dust on the way is one of those systematic effects. As the precision of cosmological measurements increase the effect of such systematic effects becomes more important to take into account. Currently there are also a tension in the value of the cosmological parameter H_0 , as two different methods produce different results. Systematic effects caused by intergalactic dust could be contributing to this tension (Mortzell et al. 2021) and understanding these effects could help in understanding this tension.

In this thesis we analysed the influence of intergalactic dust on cosmological measurements. To do this we constructed a forward model depicted in Figure 10 where we had a simulated quasar emit light through the intergalactic medium where it encountered intergalactic dust. For the quasar spectra we used a composite spectrum (see Section 7.2.1) and how the light interacted with the intergalactic dust grains is governed by the equation shown in Section 5.5. We were thus able to apply these equations to the simulated quasar spectra for a chosen redshift and dust model to create the intergalactic dust attenuated quasar spectra (see Section 7.3). For the different dust models we assumed spherical dust grains of either silicate or graphite, and could change the dust size, dust composition and Ω_{dust} for

each simulated spectra (see Sections 5.5.1 and 5.5.2). Once these algorithms were in place we could compare these simulated spectra to real observational data. This was done using SDSS observations and comparing the simulations to the observed data using colours (see Section 7.5). Lastly we did a statistical analysis for different dust models, essentially measuring the difference between the simulated colours and the colours from the observational data (see Section 7.8). The dust model that produced the smallest difference was thus the dust model that best fitted the observed data and were the dust model best portraying real intergalactic dust. To produce more definitive results improvements of the composite spectrum used in the analysis are required. Specifically surrounding the possible systematic effects.

The result of this analysis favors grains consisting of silicate with a dust grain radius around $0.1 \mu\text{m}$ and Ω_{dust} around $5 - 7 \times 10^{-6}$, which is in agreement with previous results (Johansson and Mörtzell 2012). We can therefore conclude that intergalactic dust exist and they have an effect on measurements.

10 Outlook & prospects

This work did some assumptions, and improvements on the method is possible. Since this thesis assumed equal number density of dust in all directions one could introduce a inhomogeneous distribution of dust grains mapping the distribution of galaxies to get a more accurate dust distribution model. One could use this to construct composite spectra with less possible effects from intergalactic dust, as well as taking quasars from lower redshift to construct the composites (Östman and Mörtzell 2005). It is also possible to use this distribution of dust to produce better intergalactic dust models and more accurate corrections for the effects of intergalactic dust on observations. One could also use a varying composition of different materials and grain sizes, where this thesis only assumed a certain grain material and dust grain size. There is also the possibility of further analysing the spectral features intergalactic dust causes, and look at something else besides colour to compare simulations to observations. Lastly one could also investigate the errors further, how large are the systematic effects in the composite spectrum or the SDSS data. As stated in previous sections the largest improvements of the results would come from improvements of the composite spectrum used. It would thus be fruitful to do this analysis with an improved composite spectrum.

References

- Adams, F., P. Bodenheimer, and G. Laughlin (Dec. 2005). “M dwarfs: Planet formation and long term evolution”. In: *Astronomische Nachrichten* 326, pp. 913–919. DOI: [10.1002/asna.200510440](https://doi.org/10.1002/asna.200510440).
- Aguirre, Anthony (Nov. 1999). “Intergalactic Dust and Observations of Type IA Supernovae”. In: 525.2, pp. 583–593. DOI: [10.1086/307945](https://doi.org/10.1086/307945). arXiv: [astro-ph/9904319](https://arxiv.org/abs/astro-ph/9904319) [astro-ph].
- Antonucci, Robert (Mar. 2013). “Astrophysics: Quasars still defy explanation”. In: 495.7440, pp. 165–167. DOI: [10.1038/495165a](https://doi.org/10.1038/495165a).
- Barbara Ryden (2006a). *Introduction to Cosmology. Measuring Cosmological Parameters*. Addison-Wesley, pp. 129–144.
- (2006b). *Introduction to Cosmology. Multiple/single-component universes*. Addison-Wesley.
- Bertulani, Carlos A (2013). *Nuclei in the Cosmos*. WORLD SCIENTIFIC. DOI: [10.1142/8573](https://doi.org/10.1142/8573). eprint: <https://www.worldscientific.com/doi/pdf/10.1142/8573>. URL: <https://www.worldscientific.com/doi/abs/10.1142/8573>.
- Bianchi, Simone and Andrea Ferrara (Apr. 2005). “Intergalactic medium metal enrichment through dust sputtering”. In: *Monthly Notices of the Royal Astronomical Society* 358.2, pp. 379–396. ISSN: 0035-8711. DOI: [10.1111/j.1365-2966.2005.08762.x](https://doi.org/10.1111/j.1365-2966.2005.08762.x). eprint: <https://academic.oup.com/mnras/article-pdf/358/2/379/18423159/358-2-379.pdf>. URL: <https://doi.org/10.1111/j.1365-2966.2005.08762.x>.
- Bok globule B68, ESO (2001). <https://www.eso.org/public/images/eso0102b/?lang>. Accessed: 2021-07-12.
- Cattaneo, A. et al. (July 2009). “The role of black holes in galaxy formation and evolution”. In: 460.7252, pp. 213–219. DOI: [10.1038/nature08135](https://doi.org/10.1038/nature08135). arXiv: [0907.1608](https://arxiv.org/abs/0907.1608) [astro-ph.CO].
- Draine, B. T. (Jan. 2003a). “Interstellar Dust Grains”. In: 41, pp. 241–289. DOI: [10.1146/annurev.astro.41.011802.094840](https://doi.org/10.1146/annurev.astro.41.011802.094840). arXiv: [astro-ph/0304489](https://arxiv.org/abs/astro-ph/0304489) [astro-ph].
- (Dec. 2003b). “Scattering by Interstellar Dust Grains. II. X-Rays”. In: 598.2, pp. 1026–1037. DOI: [10.1086/379123](https://doi.org/10.1086/379123). arXiv: [astro-ph/0308251](https://arxiv.org/abs/astro-ph/0308251) [astro-ph].
- Einstein, A. (1916). “Die Grundlage der allgemeinen Relativitätstheorie”. In: *Annalen der Physik* 354.7, pp. 769–822. DOI: <https://doi.org/10.1002/andp.19163540702>. eprint: <https://onlinelibrary.wiley.com/doi/pdf/10.1002/andp.19163540702>. URL: <https://onlinelibrary.wiley.com/doi/abs/10.1002/andp.19163540702>.
- Evolutionary track, Lithopsian* (2016). https://en.wikipedia.org/wiki/File:Evolutionary_track_1m.svg. Accessed: 2021-07-02.
- Friedmann, A. (Jan. 1922). “Über die Krümmung des Raumes”. In: *Zeitschrift für Physik* 10, pp. 377–386. DOI: [10.1007/BF01332580](https://doi.org/10.1007/BF01332580).
- Fukugita, M. et al. (Apr. 1996). “The Sloan Digital Sky Survey Photometric System”. In: 111, p. 1748. DOI: [10.1086/117915](https://doi.org/10.1086/117915).
- Fukugita, Masataka (Mar. 2011). “Global amount of dust in the universe”. In: *arXiv e-prints*, arXiv:1103.4191, arXiv:1103.4191. arXiv: [1103.4191](https://arxiv.org/abs/1103.4191) [astro-ph.CO].
- Gall, C., J. Hjorth, and A. C. Andersen (Sept. 2011). “Production of dust by massive stars at high redshift”. In: 19, 43, p. 43. DOI: [10.1007/s00159-011-0043-7](https://doi.org/10.1007/s00159-011-0043-7). arXiv: [1108.0403](https://arxiv.org/abs/1108.0403) [astro-ph.CO].
- Hamuy, Mario et al. (Jan. 1995). “A Hubble Diagram of Distant Type 1a Supernovae”. In: 109, p. 1. DOI: [10.1086/117251](https://doi.org/10.1086/117251).
- Henke, B.L., E.M. Gullikson, and J.C. Davis (1993). “X-Ray Interactions: Photoabsorption, Scattering, Transmission, and Reflection at $E = 50\text{--}30,000$ eV, $Z = 1\text{--}92$ ”. In: *Atomic Data and Nuclear Data Tables* 54.2, pp. 181–342. ISSN: 0092-640X. DOI: <https://doi.org/10.1006/adnd.1993.1013>. URL: <https://www.sciencedirect.com/science/article/pii/S0092640X83710132>.

- Hernquist, Lars and Volker Springel (June 2003). “An analytical model for the history of cosmic star formation”. In: 341.4, pp. 1253–1267. DOI: [10.1046/j.1365-8711.2003.06499.x](https://doi.org/10.1046/j.1365-8711.2003.06499.x). arXiv: [astro-ph/0209183](https://arxiv.org/abs/astro-ph/0209183) [astro-ph].
- Hubble, Edwin (1929). “A relation between distance and radial velocity among extra-galactic nebulae”. In: *Proceedings of the National Academy of Sciences* 15.3, pp. 168–173. ISSN: 0027-8424. DOI: [10.1073/pnas.15.3.168](https://doi.org/10.1073/pnas.15.3.168). eprint: <https://www.pnas.org/content/15/3/168.full.pdf>. URL: <https://www.pnas.org/content/15/3/168>.
- Iben Icko, Jr. (Jan. 1967). “Stellar Evolution Within and off the Main Sequence”. In: 5, p. 571. DOI: [10.1146/annurev.aa.05.090167.003035](https://doi.org/10.1146/annurev.aa.05.090167.003035).
- Inoue, Akio K. and Hideyuki Kamaya (May 2004). “Amount of intergalactic dust: constraints from distant supernovae and the thermal history of the intergalactic medium”. In: *Monthly Notices of the Royal Astronomical Society* 350.2, pp. 729–744. ISSN: 0035-8711. DOI: [10.1111/j.1365-2966.2004.07686.x](https://doi.org/10.1111/j.1365-2966.2004.07686.x). eprint: <https://academic.oup.com/mnras/article-pdf/350/2/729/3900141/350-2-729.pdf>. URL: <https://doi.org/10.1111/j.1365-2966.2004.07686.x>.
- Johansson, Joel (2015). “Sources of Dust Extinction in Type Ia Supernovae : Measurements and constraints from X-rays to the Infrared”. In: p. 78.
- Johansson, Joel and Edvard Mörtzell (Nov. 2012). “Combined constraints on intergalactic dust from quasar colours and the soft X-ray background”. In: *Monthly Notices of the Royal Astronomical Society* 426.4, pp. 3360–3368. ISSN: 0035-8711. DOI: [10.1111/j.1365-2966.2012.21940.x](https://doi.org/10.1111/j.1365-2966.2012.21940.x). eprint: <https://academic.oup.com/mnras/article-pdf/426/4/3360/3337614/426-4-3360.pdf>. URL: <https://doi.org/10.1111/j.1365-2966.2012.21940.x>.
- Karttunen H. et al. (2017). *Fundamental Astronomy. Variable Stars*. Springer, pp. 299–312.
- King, Ivan (May 1952). “A Note on the Concept of Effective Wave Length.” In: 115, pp. 580–582. DOI: [10.1086/145583](https://doi.org/10.1086/145583).
- Kjellqvist, Jimmy (2021). *Foundation for an analysis of the dust of the Nearby Universe*. URL: <https://www.diva-portal.org/smash/get/diva2:1539544/FULLTEXT01.pdf>.
- Lambourne, R.J. (2010). *Relativity, Gravitation and Cosmology*. Relativity, Gravitation and Cosmology. Cambridge University Press. ISBN: 97805211131384. URL: <https://books.google.se/books?id=GUySYQaDM1cC>.
- Laor, Ari and Bruce T. Draine (Jan. 1993). “Spectroscopic Constraints on the Properties of Dust in Active Galactic Nuclei”. In: 402, p. 441. DOI: [10.1086/172149](https://doi.org/10.1086/172149).
- Laughlin, Gregory, Peter Bodenheimer, and Fred C. Adams (June 1997). “The End of the Main Sequence”. In: *The Astrophysical Journal* 482.1, pp. 420–432. DOI: [10.1086/304125](https://doi.org/10.1086/304125). URL: <https://doi.org/10.1086/304125>.
- Loeb, Abraham and Zoltan Haiman (Dec. 1997). “Signatures of Intergalactic Dust from the First Supernovae”. In: *The Astrophysical Journal* 490.2, pp. 571–576. DOI: [10.1086/304919](https://doi.org/10.1086/304919). URL: <https://doi.org/10.1086/304919>.
- Lyke, Brad W. et al. (Sept. 2020). “The Sloan Digital Sky Survey Quasar Catalog: Sixteenth Data Release”. In: 250.1, 8, p. 8. DOI: [10.3847/1538-4365/aba623](https://doi.org/10.3847/1538-4365/aba623). arXiv: [2007.09001](https://arxiv.org/abs/2007.09001) [astro-ph.GA].
- Main Sequence, Universe Today* (2010). <https://www.universetoday.com/52252/main-sequence/>. Accessed: 2021-07-02.
- Mathis, J. S., W. Rumpl, and K. H. Nordsieck (Oct. 1977). “The size distribution of interstellar grains.” In: 217, pp. 425–433. DOI: [10.1086/155591](https://doi.org/10.1086/155591).
- Mathis, John S. and C. -W. Lee (Aug. 1991). “X-Ray Halos as Diagnostics of Interstellar Grains”. In: 376, p. 490. DOI: [10.1086/170297](https://doi.org/10.1086/170297).
- Mazzali, Paolo A. et al. (Feb. 2007). “A Common Explosion Mechanism for Type Ia Supernovae”. In: *Science* 315.5813, p. 825. DOI: [10.1126/science.1136259](https://doi.org/10.1126/science.1136259). arXiv: [astro-ph/0702351](https://arxiv.org/abs/astro-ph/0702351) [astro-ph].

- Ménard, Brice et al. (June 2010). “Measuring the galaxy-mass and galaxy-dust correlations through magnification and reddening”. In: 405.2, pp. 1025–1039. DOI: [10.1111/j.1365-2966.2010.16486.x](https://doi.org/10.1111/j.1365-2966.2010.16486.x). arXiv: [0902.4240](https://arxiv.org/abs/0902.4240) [astro-ph.CO].
- Mortsell, Edvard et al. (May 2021). “The Hubble Tension Bites the Dust: Sensitivity of the Hubble Constant Determination to Cepheid Color Calibration”. In: *arXiv e-prints*, arXiv:2105.11461, arXiv:2105.11461. arXiv: [2105.11461](https://arxiv.org/abs/2105.11461) [astro-ph.CO].
- Mörtsell, Edvard and Ariel Goobar (Sept. 2003). “Constraints on intergalactic dust from quasar colours”. In: 2003.9, 009, p. 009. DOI: [10.1088/1475-7516/2003/09/009](https://doi.org/10.1088/1475-7516/2003/09/009). arXiv: [astro-ph/0308046](https://arxiv.org/abs/astro-ph/0308046) [astro-ph].
- Östman, Linda and Edvard Mörtsell (Feb. 2005). “Limiting the dimming of distant type Ia supernovae”. In: 2005.2, 005, p. 005. DOI: [10.1088/1475-7516/2005/02/005](https://doi.org/10.1088/1475-7516/2005/02/005). arXiv: [astro-ph/0410501](https://arxiv.org/abs/astro-ph/0410501) [astro-ph].
- Pearson, Karl (1900). “X. On the criterion that a given system of deviations from the probable in the case of a correlated system of variables is such that it can be reasonably supposed to have arisen from random sampling”. In: *The London, Edinburgh, and Dublin Philosophical Magazine and Journal of Science* 50.302, pp. 157–175. DOI: [10.1080/14786440009463897](https://doi.org/10.1080/14786440009463897). eprint: <https://doi.org/10.1080/14786440009463897>. URL: <https://doi.org/10.1080/14786440009463897>.
- Peng, C. Y. et al. (Oct. 1999). “The Quasar Pair Q1634+267A,B and the Binary QSO versus Dark Lens Hypotheses”. In: 524.2, pp. 572–581. DOI: [10.1086/307860](https://doi.org/10.1086/307860). arXiv: [astro-ph/9904426](https://arxiv.org/abs/astro-ph/9904426) [astro-ph].
- Phillips, M. M. (Aug. 1993). “The Absolute Magnitudes of Type IA Supernovae”. In: 413, p. L105. DOI: [10.1086/186970](https://doi.org/10.1086/186970).
- Planck Collaboration et al. (Sept. 2020). “Planck 2018 results. VI. Cosmological parameters”. In: 641, A6, A6. DOI: [10.1051/0004-6361/201833910](https://doi.org/10.1051/0004-6361/201833910). arXiv: [1807.06209](https://arxiv.org/abs/1807.06209) [astro-ph.CO].
- Pyphot*, M. Fouesneau (2016). <https://mfouesneau.github.io/docs/pyphot/>. Accessed: 2021-05-12.
- Richards, Gordon T. et al. (May 2001). “Colors of 2625 Quasars at $0 < Z < 5$ Measured in the Sloan Digital Sky Survey Photometric System”. In: 121.5, pp. 2308–2330. DOI: [10.1086/320392](https://doi.org/10.1086/320392). arXiv: [astro-ph/0012449](https://arxiv.org/abs/astro-ph/0012449) [astro-ph].
- Riess, Adam G. et al. (July 2016). “A 2.4% Determination of the Local Value of the Hubble Constant”. In: 826.1, 56, p. 56. DOI: [10.3847/0004-637X/826/1/56](https://doi.org/10.3847/0004-637X/826/1/56). arXiv: [1604.01424](https://arxiv.org/abs/1604.01424) [astro-ph.CO].
- Ryan, Sean G. and Andrew J. Norton (2010). *Stellar Evolution and Nucleosynthesis*. Course reader for Open University course S382 Astrophysics. Cambridge: Cambridge University Press. URL: <http://oro.open.ac.uk/28529/>.
- Sackmann, I. -Juliana, Arnold I. Boothroyd, and Kathleen E. Kraemer (Nov. 1993). “Our Sun. III. Present and Future”. In: 418, p. 457. DOI: [10.1086/173407](https://doi.org/10.1086/173407).
- Schneider, Donald P. et al. (June 2010). “The Sloan Digital Sky Survey Quasar Catalog. V. Seventh Data Release”. In: 139.6, 2360, p. 2360. DOI: [10.1088/0004-6256/139/6/2360](https://doi.org/10.1088/0004-6256/139/6/2360). arXiv: [1004.1167](https://arxiv.org/abs/1004.1167) [astro-ph.CO].
- Smith, Randall K. and Eli Dwek (Aug. 1998). “Soft X-Ray Scattering and Halos from Dust”. In: *The Astrophysical Journal* 503.2, pp. 831–842. DOI: [10.1086/306018](https://doi.org/10.1086/306018). URL: <https://doi.org/10.1086/306018>.
- Star Life Cycle Chart*, R.N. Bailey (2017). https://en.wikipedia.org/wiki/File:Star_Life_Cycle_Chart.jpg. Accessed: 2021-07-02.
- Telfer, Randal C. et al. (Feb. 2002). “The Rest-Frame Extreme-Ultraviolet Spectral Properties of Quasi-stellar Objects”. In: 565.2, pp. 773–785. DOI: [10.1086/324689](https://doi.org/10.1086/324689). arXiv: [astro-ph/0109531](https://arxiv.org/abs/astro-ph/0109531) [astro-ph].

- Tokunaga, A. T. and W. D. Vacca (Apr. 2005). “The Mauna Kea Observatories Near-Infrared Filter Set. III. Isophotal Wavelengths and Absolute Calibration”. In: *Publications of the Astronomical Society of the Pacific* 117.830, pp. 421–426. DOI: [10.1086/429382](https://doi.org/10.1086/429382). URL: <https://doi.org/10.1086/429382>.
- Tripp, Robert (Mar. 1998). “A two-parameter luminosity correction for Type IA supernovae”. In: 331, pp. 815–820.
- Vanden Berk, Daniel E. et al. (Aug. 2001). “Composite Quasar Spectra from the Sloan Digital Sky Survey”. In: 122.2, pp. 549–564. DOI: [10.1086/321167](https://doi.org/10.1086/321167). arXiv: [astro-ph/0105231](https://arxiv.org/abs/astro-ph/0105231) [[astro-ph](https://arxiv.org/abs/astro-ph)].
- William C. Keel (2007). *The Road to Galaxy Formation*. Springer, Berlin, Heidelberg.
- Wu, W. L. Kimmy et al. (July 2020). “Hubble constant difference between CMB lensing and BAO measurements”. In: 102.2, 023510, p. 023510. DOI: [10.1103/PhysRevD.102.023510](https://doi.org/10.1103/PhysRevD.102.023510). arXiv: [2004.10207](https://arxiv.org/abs/2004.10207) [[astro-ph](https://arxiv.org/abs/astro-ph).C0].
- Xiang, Maosheng et al. (Aug. 2018). “Stellar Mass Distribution and Star Formation History of the Galactic Disk Revealed by Mono-age Stellar Populations from LAMOST”. In: *The Astrophysical Journal Supplement Series* 237.2, p. 33. DOI: [10.3847/1538-4365/aad237](https://doi.org/10.3847/1538-4365/aad237). URL: <https://doi.org/10.3847/1538-4365/aad237>.

A Results of Model 1

All of the plots shown below are the results from Section 7 but with Model 1 instead of Model 2.

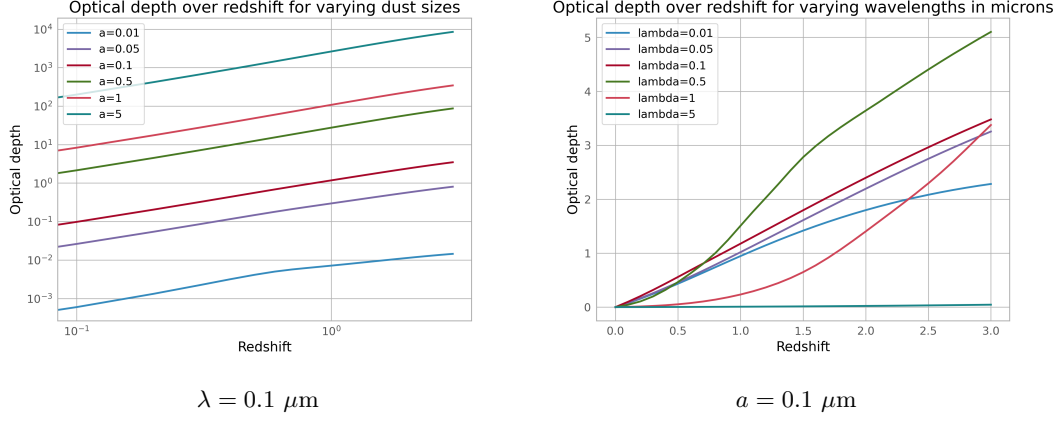


Figure 27: The optical depth as a function of redshift, $\tau(z)$. First plot with constant wavelength and varying dust size and the second plot with constant dust size and varying wavelength. Both the dust grain size and wavelength are in μm units.

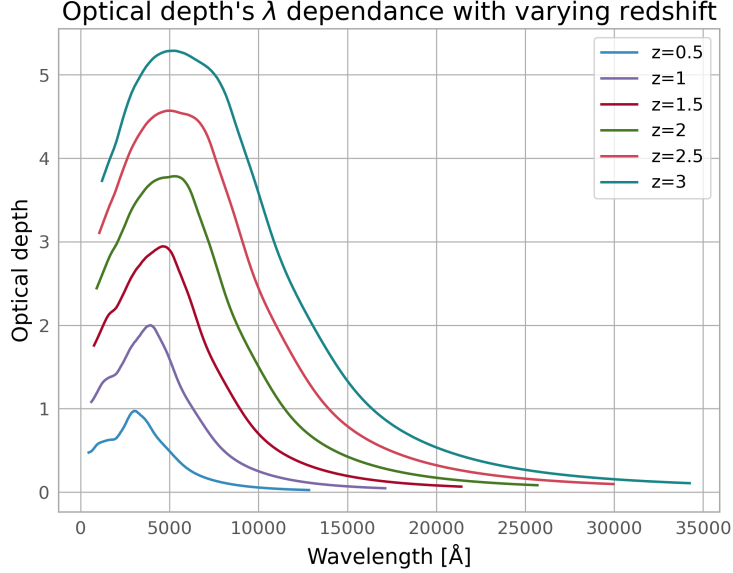


Figure 28: How the optical depth depends on wavelength with varying redshift for silicates.

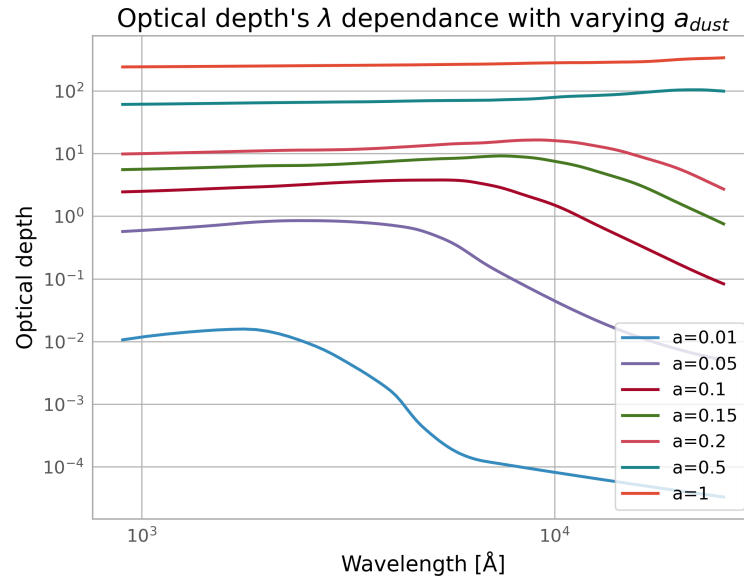


Figure 29: How the optical depth depends on wavelength with varying dust size in μm for silicates.

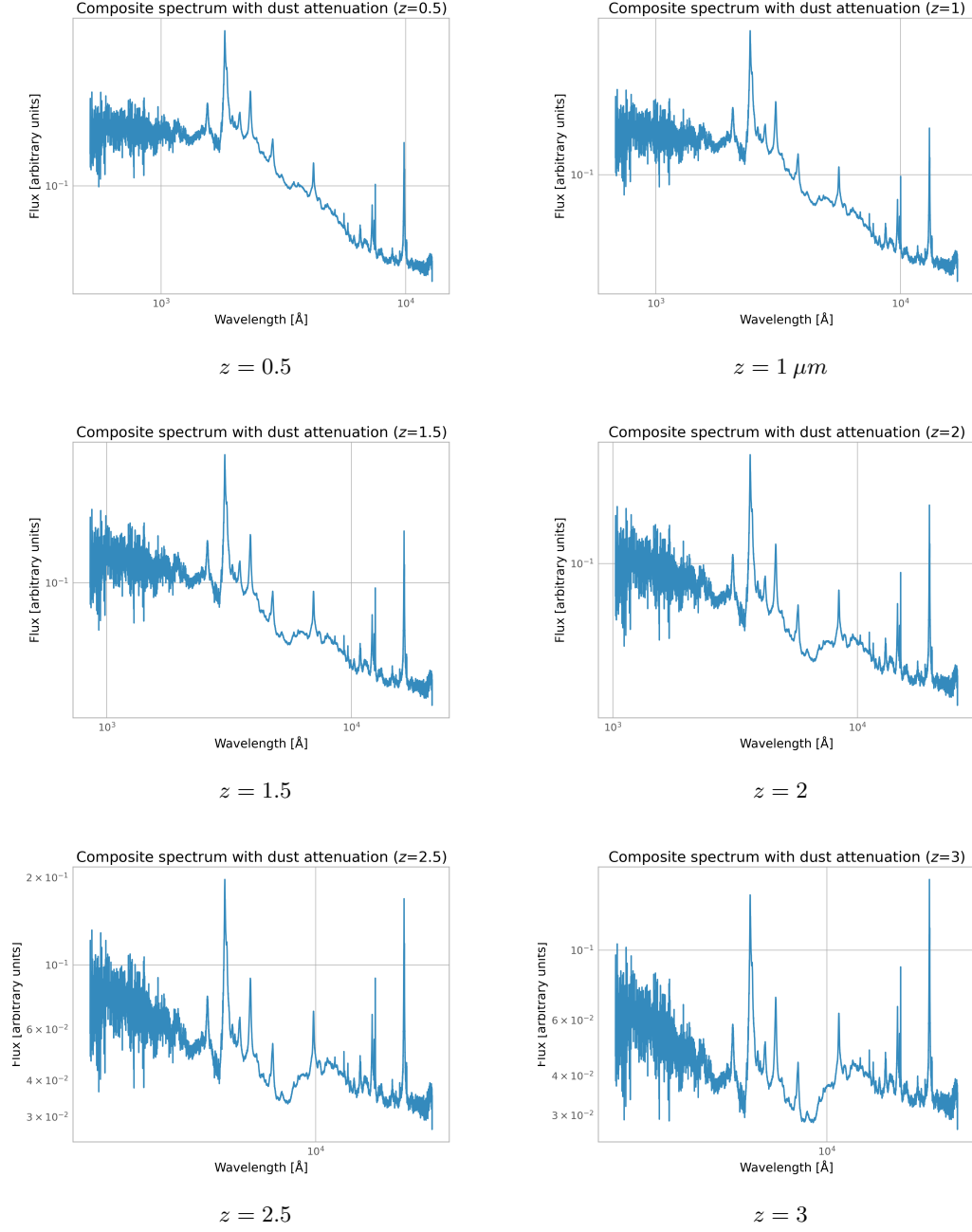
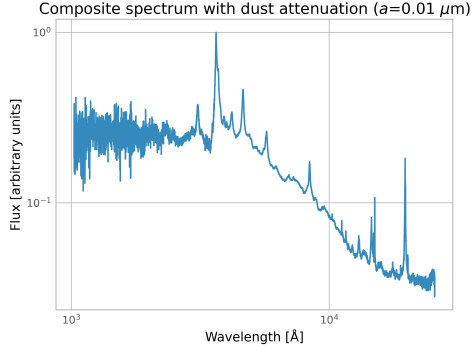
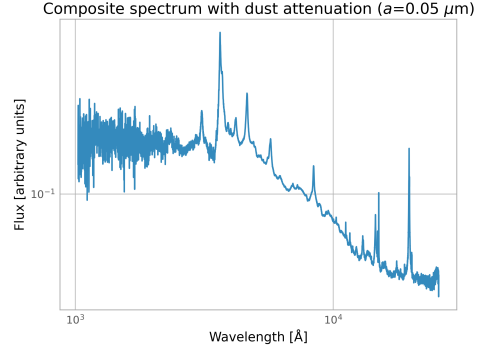


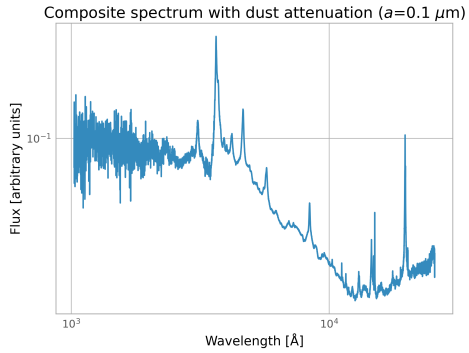
Figure 30: Composite spectra with dust attenuation caused by silicates for varying redshifts. All of the spectra has a dust size of $a_{dust} = 0.1 \mu m$.



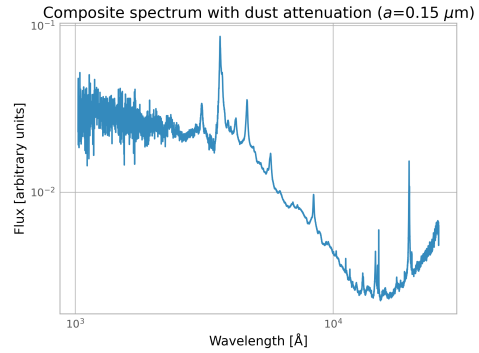
$$a_{dust} = 0.01 \mu\text{m}$$



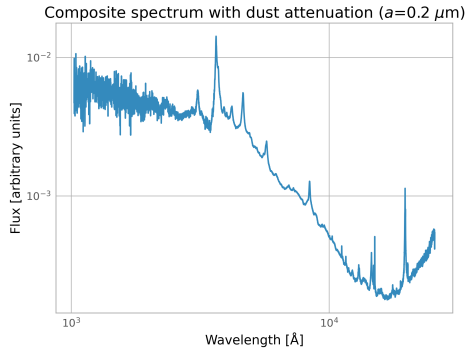
$$a_{dust} = 0.05 \mu\text{m}$$



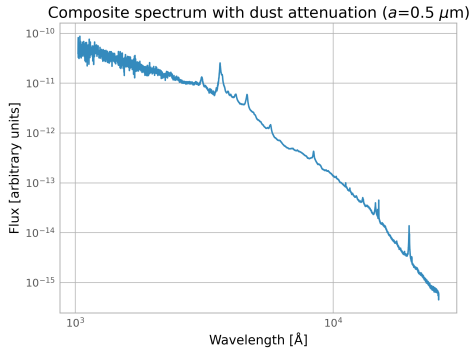
$$a_{dust} = 0.1 \mu\text{m}$$



$$a_{dust} = 0.15 \mu\text{m}$$

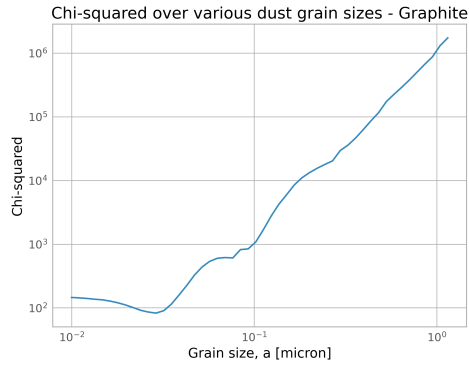


$$a_{dust} = 0.2 \mu\text{m}$$

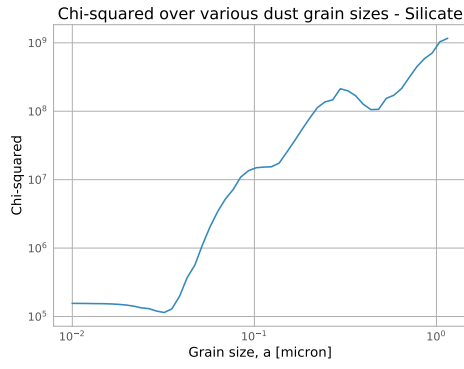


$$a_{dust} = 0.5 \mu\text{m}$$

Figure 31: Composite spectra with dust attenuation caused by silicates for varying dust sizes. All of the spectra has a redshift $z = 2$.

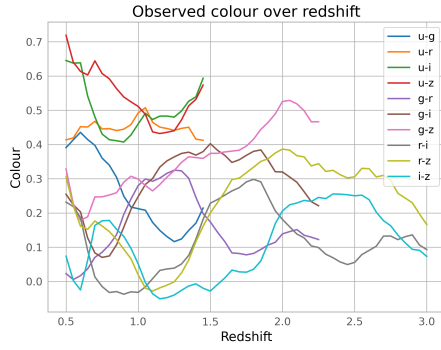


Graphite

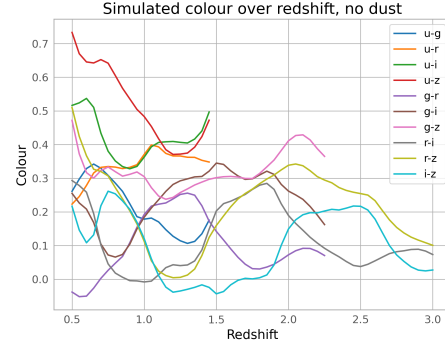


Silicate

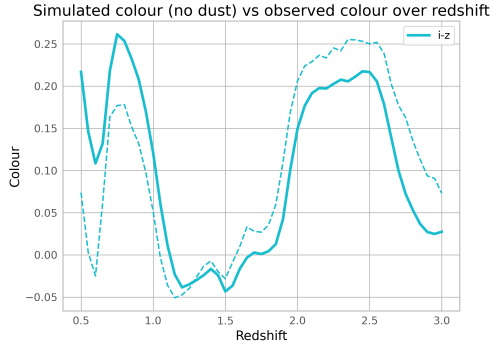
Figure 32: The results from the χ^2 calculations for both graphite and silicate. This is a measure of the how closely the dust model matches observations where the smaller χ^2 the better that model fits to observations.



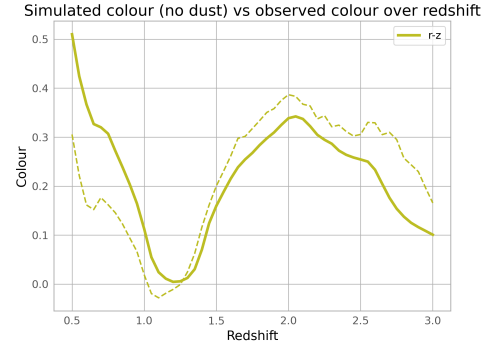
The observed colours for each redshift bin.



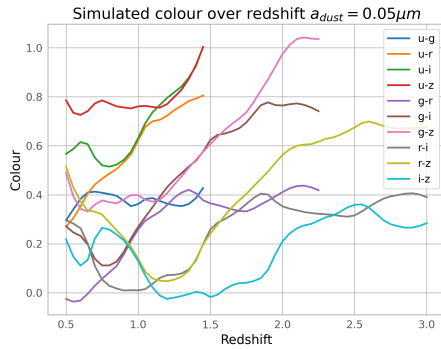
The simulated colours for the composite spectrum without dust attenuation.



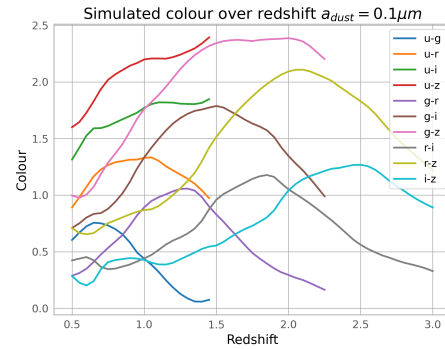
Comparison between the observed (dashed) and the simulated with no dust attenuation (full) i-z colour.



Comparison between the observed (dashed) and the simulated with no dust attenuation (full) r-z colour.



Simulated colours with dust attenuation with grain size $a_{dust} = 0.05 \mu m$



Simulated colours with dust attenuation with grain size $a_{dust} = 0.1 \mu m$

Figure 33: Several plots showing the result of the colour calculations, along with some comparisons between the observed and the simulated for the composite spectrum with no dust attenuation.)